

Banner appropriate to article type will appear here in typeset article

No-slip, slip and friction at fluid-solid interfaces: Concept of adsorption layer

Haodong Zhang^{1,2}, Fei Wang^{1,2} †, and Britta Nestler^{1,2,3}

¹Institute of Applied Materials-Microstructure Modelling and Simulation, Karlsruhe Institute of Technology (KIT), Strasse am Forum 7, Karlsruhe 76131, Germany

²Institute of Nanotechnology, Karlsruhe Institute of Technology (KIT), Hermann-von-Helmholtz-Platz 1, Eggenstein-Leopoldshafen 76344, Germany

³Institute of Digital Materials Science, Karlsruhe University of Applied Sciences, Moltkestrasse 30, Karlsruhe 76133, Germany

(Received xx; revised xx; accepted xx)

When a fluid contacts solid surfaces, it can spread or slide, and the motion of the contact line involves a complex interplay between hydrodynamic and thermodynamic effects. Hydrodynamic theories, like the Huh & Scriven and Cox & Voinov models, assume a no-slip boundary condition, neglecting the macroscopic fluid slip at the fluid-solid interface. However, they cannot explain the contact line motion during droplet spreading which in thermodynamic theories is attribute to the microscopic surface diffusion of fluid molecules. To bridge these perspectives, we heed the physical origin of slip phenomenon by employing energy minimization principles to establish a force balance between solid-fluid friction, thermodynamic force, and viscous stress at the fluid-solid contact region. Our analysis reveals that slip is an intrinsic property, just like molecular surface diffusion, is also governed by fluid-solid intermolecular interactions. Based on our model with slip, we extend the classical Huh & Scriven and Cox & Voinov theories by incorporating friction, enabling a more comprehensive understanding of droplet slide and kinetic induced contact angle hysteresis (CAH). Our results demonstrate that solid-fluid friction plays a vital role in momentum transfer between the substrate and the droplet, therefore, modifies the droplet internal fluid flow during wetting drastically. Under strong friction, classical wetting predictions with CAH are recovered, whereas weak friction suppresses internal fluid motion, leading to the disappearance of CAH. These findings provide new insights into wetting dynamics, highlighting the importance of friction in slip behavior. This work has broad implications for droplet transport, surface engineering, and applications in microfluidics and coatings.

Key words:

† Email address for correspondence: fei.wang@kit.edu

1. Introduction

When fluids are in contact with solid substrates, various boundary layers emerge at the fluid-solid interface. In multicomponent fluids, intermolecular interactions with the substrate can lead to depletion or adsorption layers on the microscopic scale, (De Gennes 1981; Wang *et al.* 2023; Zhang *et al.* 2024c) which influence macroscopic wetting and dewetting behaviors. Furthermore, when the fluid flows, its relative motion is damped by the solid wall, causing a velocity gradient near the fluid-solid interface (Xia 2024; Hadjiconstantinou 2024). This velocity boundary layer is generally categorized into two main types:

- *No-Slip Boundary Condition* (Lauga *et al.* 2005; Luchini 2013; Wen *et al.* 2022). From a macroscopic perspective, numerous experiments support the no-slip boundary condition,

$$\mathbf{u}_s = \mathbf{0}. \quad (1.1)$$

which has been regarded as a fundamental principle in fluid mechanics. With the advent of computational fluid dynamics, the no-slip condition became the standard assumption due to its predictive precision (Qian *et al.* 2008; Yue & Feng 2012; Krüger *et al.* 2017; Lim *et al.* 2019; Yue 2020; Ding & Xia 2023). However, this assumption leads to a paradox in wetting dynamics: If the velocity at the droplet-substrate interface were strictly zero, the fluid molecules would remain stationary, contradicting experimental observations of the droplet spreading and retraction. Qian *et al.* (2006); Yue *et al.* (2010) addressed this issue through numerical simulations, showing that droplet motion arises from molecular diffusion at the solid-fluid interface rather than classical advection. This provides a solid explanation for the velocity boundary layer.

- *Slip boundary condition* (Lauga & Stone 2003; Jung *et al.* 2016; Kusumaatmaja *et al.* 2016; Bae *et al.* 2019; Yariv 2023). Recent experiments at sub-micrometer and nanometer scales have revealed that slip velocity at the fluid-solid interface does exist (Neto *et al.* 2005; Myers 2011; Maali & Bhushan 2012; Xie *et al.* 2018). Molecular dynamics (MD) simulations also confirm that fluid molecules can slip (Qian *et al.* 2003, 2006; Voronov *et al.* 2006; Kumar Kannam *et al.* 2012; Ramos-Alvarado *et al.* 2016; Alipour *et al.* 2019). These findings challenge the universality of the no-slip condition. In fact, the concept of slip is not new; it dates back to the 19th century, when Navier and Maxwell introduced the slip length l_s to characterize the slip velocity \mathbf{u}_s (Navier 1822; Maxwell 1879; Coron 1996) as

$$\mathbf{u}_s = l_s \partial_n \mathbf{u}. \quad (1.2)$$

The value of l_s ranges from nanometers to micrometers in experiments (Joseph & Tabeling 2005; Muralidhar *et al.* 2011), depending on fluid-substrate properties. Additionally, l_s is highly sensitive to flow geometry; for instance, slip in carbon nanotubes (Secchi *et al.* 2016) is orders of magnitude larger than that observed in macroscopic systems. However, few fundamental questions remain: What governs the transition between slip and no-slip conditions? Why do some fluids slip while others adhere? Why do nanometer-scale droplets exhibit significant slip while macroscopic drops do not?

A key mechanism for suppressing slip is the solid-fluid friction (Petrvac & Harrowell 2007; Cross *et al.* 2018; Li *et al.* 2023). In everyday life, we have experienced that friction allows vehicles to stop when braking. Similarly, at the fluid-solid interface, velocity damping occurs due to friction, which is quantified by the friction coefficient λ . In principle, if λ goes to infinity, the no-slip condition ($l_s = 0$) is enforced, while $\lambda = 0$ corresponds to perfect slip ($l_s \rightarrow \infty$). However, the physical magnitude of λ remains uncertain. To address this, Bocquet & Barrat (1994) linked friction to velocity dissipation in the boundary layer using *linear response theory*. They related λ to the dynamic autocorrelation function, drawing an analogy to transport coefficients via the Green-Kubo relation. In their framework, friction

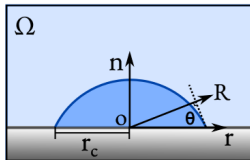


Figure 1: Sessile droplet with contact radius r_c attaches the gray substrate, \mathbf{n} and \mathbf{r} guides the substrate normal and tangential directions, respectively.

emerges as a dissipation mechanism for *kinetic energy perturbations*, consistent with the fluctuation-dissipation theorem. But, a crucial question is unresolved: For a partially wetted multicomponent droplet, where chemical free energy fluctuates and surface tension influences the macroscopic flow motion, how does friction respond linearly to these complex factors?

In this study, we explore the interplay between solid-fluid friction, surface tension, and viscous stress from an energy minimization perspective. We focus on multicomponent fluid systems, integrating thermodynamic insights (Yue *et al.* 2010; Xu *et al.* 2018) with hydrodynamic theories (Ren *et al.* 2015; Hadjiconstantinou 2021) to develop a more comprehensive understanding of the slip phenomenon. Furthermore, we examine the molecular origins of friction by analyzing fluid-solid interactions. Based on this, we formulate a generalized energy dissipation law at the fluid-solid interface, which plays a pivotal role in determining slip behavior of several conventional flow scenarios, including Poiseuille flow, Couette flow, wedge flow, droplet slide, and so on.

This paper is structured as follows: Section 2 presents the total energy functional formulation, including contributions from chemical free energy, potential energy, and kinetic energy. Section 3 derives evolution equations governing wetting dynamics based on energy minimization principles. Section 4 discusses the fundamental mechanisms underlying friction at the fluid-solid interface, including a Green-Kubo relation analysis and a molecular-scale perspective. Section 5 examines the steady-state behaviors of wetting, highlighting equilibrium conditions and flow structures near the contact line. Finally, Section 6 presents case studies on single-phase flow, wedge flow dynamics, and droplet sliding.

2. Total energy functional

Considering the multi-component system with droplets contacting solid substrate, the *fluid* has the total energy density functional \mathcal{L} consisted of three parts, namely, the chemical free energy functional \mathcal{F} , the potential energy \mathcal{P} , and the kinetic energy \mathcal{K} ,

$$\mathcal{L} = \mathcal{F} + \mathcal{P} + \mathcal{K}.$$

Additionally, the kinetic energy of the *solid substrate* \mathcal{K}_w also needs to be considered. Thus, the total energy density functional of the fluid and substrate system reads,

$$\mathcal{L}_T = \mathcal{L} + \mathcal{K}_w.$$

2.1. Chemical free energy functional

The fluid chemical free energy functional \mathcal{F} is formulated as the summation of the bulk free energy functional in the bulk fluid domain Ω , and the wall energy functional at the fluid-solid contact surface L as,

$$\mathcal{F} = \int_{\Omega} g \, d\Omega + \int_L g_w \, \delta l \, dL. \quad (2.1)$$

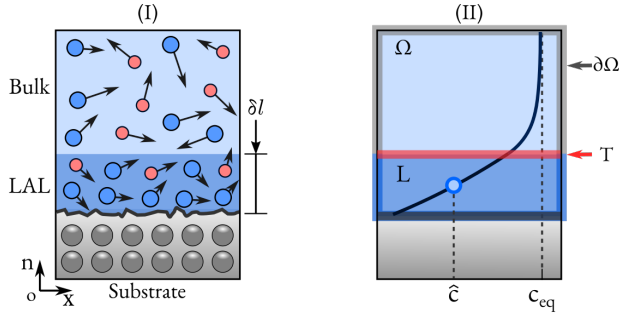


Figure 2: (I) 2D illustration of the multicomponent fluid contacting the gray solid substrate. The mid blue Langmuir adsorption layer (LAL) with thickness δl forms between the gray substrate and the light blue bulk fluid. (II) The LAL composition \hat{c} deviates from the bulk equilibrium composition c_{eq} due to the solid-fluid interactions.

Especially, in this work, we specify the thin layer at the fluid-solid contact region with the thickness δl and denominate it as the Langmuir adsorption layer (LAL). This thin layer denotes the region where solid and fluid interactions exist, resulting in the adsorption and depletion of the fluid molecules. For different fluid-solid pairs, the magnitude of δl ranges from several nanometer to micro-meter scales (Butt *et al.* 2018; Wang & Nestler 2024b), which not only depends on the properties of the fluid solid interactions, but also relies on the size of the molecules.

2.1.1. Chemical free energy in bulk fluids

In Eq. (2.1), the bulk free energy density functional takes the Cahn-Hilliard formulation (Cahn & Hilliard 1958; Christianto *et al.* 2022; Zhang *et al.* 2022)

$$g = f(\mathbf{c}) + \sum_i (\kappa/2) (\nabla c_i)^2,$$

in which the spatial-temporal fluid composition is defined by $\mathbf{c}(\mathbf{x}, t) = (c_1, c_2, \dots, c_i, \dots)$. The bulk free energy density f is assigned with the regular solution model, yielding

$$f(\mathbf{c}) = (k_B T / v_m) \sum_i (c_i \ln c_i + \sum_j \chi_{ij} c_i c_j).$$

The parameters k_B , T , and v_m represent the Boltzmann constant, temperature, and lattice volume, respectively. The molecular interaction between fluid molecules is quantified by χ_{ij} , as $\chi_{ij} > 0 (< 0)$ denotes the repulsion (attraction). The parameter κ scales the fluid-fluid interfacial tension.

2.1.2. Chemical free energy in LAL

In Eq. (2.1), the second integrand scales the chemical interaction between the fluid and the solid substrate, and is related with the combination of entropy density s_w , enthalpy density h_w and van der Waals interaction f_{vdw} (Wang *et al.* 2024; De Gennes 1985) as,

$$f_w = h_w(\mathbf{c}) - T s_w(\mathbf{c}) + f_{vdw}.$$

Noteworthy, f_{vdw} between solid and fluid molecules alters the free energy of fluid molecules and can be calculated with the Lennard-Jones type of potential energy density as

$$f_{vdw} = \sum_i \epsilon c_i (\sigma_i / r^m - \sigma_i / r^n),$$

where ϵ is the depth of the potential well, and σ_i is the distance at which the potential energy is zero. The scaling parameters m and n are obtained from experiments. Apparently, we can

assume that the total van der Waals force is composition dependent. In this way, we use the averaged composition \bar{c}_i of LAL to express the wall energy density as,

$$f_w = (k_B T / v_m) \sum_i (\bar{c}_i \ln \bar{c}_i + \chi_i^w \bar{c}_i + \sum_j \chi_{ij}^w \bar{c}_i \bar{c}_j). \quad (2.2)$$

The fluid molecules in LAL are constraint by the wall energy density function f_w which differs from the bulk free energy density f . Consequently, when the fluid contacts the solid substrate, f_w and f should be balanced in both LAL and bulk fluid. Resulting from this, the adsorption/depletion scenarios appear with the composition decay/increase from LAL to the bulk region, as shown in figure 2(II). This surface composition variance also lead to the excess energy which is obtained by the method developed in our previous work Cai *et al.* (2024). By defining the thickness of LAL δl as the characteristic length scale of solid-fluid intermolecular forces, the total chemical free energy functional Eq. (2.1) is formulated with

$$\mathcal{F} = \int_{\Omega} \left[f(\mathbf{c}) + \sum_i (\kappa/2) (\nabla c_i)^2 \right] d\Omega + \int_L \left[f_w(\bar{c}_i) + \sum_i (\kappa'/2) (\nabla_s \bar{c}_i)^2 \right] \delta l dL, \quad (2.3)$$

where the surface gradient operator is defined as $\nabla_s := \nabla - \mathbf{n}(\mathbf{n} \cdot \nabla)$ with respect to the normal vector of the solid substrate, \mathbf{n} . This chemical free energy functional is consistent with the dynamical boundary condition models by Liu *et al.* (2024). The physical meaning of κ' will be elucidated in Sec. 5.1.

2.2. Potential energy and kinetic energy

For the multi-component fluid flow, the potential energy of the fluid is represented by

$$\mathcal{P} = \int_{\Omega} p d\Omega + \int_L \bar{p} \delta l dL. \quad (2.4)$$

Here, the pressure density in bulk and LAL are labeled by p and \bar{p} , respectively. The fluid kinetic energy takes the following formulation with the macroscopic fluid velocity \mathbf{u} inside the bulk region, and $\bar{\mathbf{u}}$ in LAL,

$$\mathcal{K} = \int_{\Omega} \frac{\rho \mathbf{u}^2}{2} d\Omega + \int_L \frac{\rho \bar{\mathbf{u}}^2}{2} \delta l dL, \quad (2.5)$$

where the density ρ is assumed to be constant and the fluid velocity $\bar{\mathbf{u}}$ in LAL assigns the average value for the fluid molecules.

3. Evolution equations by energy minimization

In this section, we derive the proper evolution equations for the system, based on the energy minimization method discussed in our previous works (Zhang *et al.* 2024a; Wang & Nestler 2024a). For the sake of brevity, only the crucial deductions are presented.

3.1. Chemical free energy functional dissipation

Starting from the temporal decay of the chemical free energy functional \mathcal{F} ,

$$d\mathcal{F}/dt = \int_{\Omega} \sum_i \left[\left(\frac{\partial f}{\partial c_i} - \kappa \nabla^2 c_i \right) \frac{dc_i}{dt} + \nabla \cdot (\kappa \nabla c_i \otimes \nabla c_i) \cdot \mathbf{u} \right] d\Omega - \int_{\partial\Omega} \sum_i (\kappa \nabla \bar{c}_i \cdot \mathbf{n}) \frac{d\bar{c}_i}{dt} dL \quad (3.1)$$

$$+ \int_L \sum_i \left[\left(\frac{\partial f_w}{\partial \bar{c}_i} - \kappa' \nabla_s^2 \bar{c}_i \right) \frac{d\bar{c}_i}{dt} + \nabla_s \cdot (\kappa' \nabla_s \bar{c}_i \otimes \nabla_s \bar{c}_i) \cdot \bar{\mathbf{u}} \right] \delta l dL. \quad (3.2)$$

The second integral in Eq. (3.1) is obtained from the divergence theorem and the well-known equality of vector calculus, $\nabla \cdot (\kappa \nabla c_i \otimes \nabla c_i) = \nabla \cdot (\kappa \nabla c_i) \nabla c_i + \kappa \nabla c_i \cdot \nabla \nabla c_i$. Physically,

Eqs. (3.1) and (3.2) describe the chemical free energy dissipation via bulk diffusion and surface diffusion in LAL, respectively.

3.2. Potential energy dissipation

The potential energy dissipation follows the simple chain rule,

$$d\mathcal{P}/dt = \int_{\Omega} \frac{dp}{dx} \cdot \frac{dx}{dt} d\Omega + \int_L \frac{d\bar{p}}{dx} \cdot \frac{dx}{dt} \delta l dL = \int_{\Omega} \nabla p \cdot \mathbf{u} d\Omega + \int_L \nabla \bar{p} \cdot \bar{\mathbf{u}} \delta l dL. \quad (3.3)$$

3.3. Kinetic energy dissipation

The kinetic energy dissipation is calculated with the total derivatives as,

$$d\mathcal{K}/dt = \int_{\Omega} \rho \mathbf{u} \cdot d\mathbf{u}/dt d\Omega + \int_L \rho \bar{\mathbf{u}} \cdot d\bar{\mathbf{u}}/dt \delta l dL. \quad (3.4)$$

In bulk fluid Ω , we apply the vector calculus and express the force balance,

$$\rho d\mathbf{u}/dt = \mathbf{f} + \nabla(\zeta \nabla \cdot \mathbf{u}) + \nabla \cdot \underline{\underline{\mathbf{T}}}, \quad (3.5)$$

The force \mathbf{f} exerted on the fluid takes the tensor formation $\mathbf{f} = -\nabla \cdot (\mathbf{P}\mathbf{I} + \underline{\underline{\Theta}})$, which contains the grand potential P and the surface stress tensor $\underline{\underline{\Theta}}$ reading

$$P = p - g + \sum_i (\delta g / \delta c_i) c_i, \quad \underline{\underline{\Theta}} = -[g - \sum_i (\delta g / \delta c_i) c_i] \mathbf{I} + \sum_i \kappa \nabla c_i \otimes \nabla c_i.$$

The second term on the right hand side (*rhs*) of Eq. (3.5) describes the compressibility of the fluid scaled by the volume viscosity ζ . In this work, the fluid is incompressible, so that $\nabla \cdot \mathbf{u} = 0$ becomes an individual equation. The last term in Eq. (3.5) denotes the diffusion of fluid velocity which is actually the viscous dissipation with the viscosity η . Due to the angular momentum conservation, the fluid viscous stress adopts the symmetric tensor as,

$$\underline{\underline{\mathbf{T}}} = \eta (\nabla \mathbf{u} + \nabla \mathbf{u}^T).$$

After simplification, the Navier-Stokes equations (NaSt) in the bulk fluid are derived,

$$\begin{aligned} \nabla \cdot \mathbf{u} &= 0, \\ \rho d\mathbf{u}/dt &= -\nabla \cdot (\mathbf{P}\mathbf{I} + \underline{\underline{\Theta}}) + \nabla \cdot \underline{\underline{\mathbf{T}}}. \end{aligned} \quad (3.6)$$

Substituting NaSt into Eq. (3.4), the kinetic energy decay is simplified as

$$d\mathcal{K}/dt = - \int_{\Omega} \left[\nabla \cdot (\mathbf{P}\mathbf{I} + \underline{\underline{\Theta}}) \cdot \mathbf{u} + \underline{\underline{\mathbf{T}}} : \nabla \mathbf{u} \right] d\Omega - \int_{\partial\Omega} \underline{\underline{\mathbf{T}}} \cdot \mathbf{n} \cdot \bar{\mathbf{u}} dL - \int_L \rho d\bar{\mathbf{u}}/dt \cdot \bar{\mathbf{u}} \delta l dL. \quad (3.7)$$

Here, the second integral in Eq. (3.7) hinges the viscous stress between bulk and LAL at $\partial\Omega \equiv L$, and is obtained by the divergence theorem with $(\nabla \cdot \underline{\underline{\mathbf{T}}}) \cdot \mathbf{u} = \nabla \cdot (\underline{\underline{\mathbf{T}}} \mathbf{u}) - \underline{\underline{\mathbf{T}}} : \nabla \mathbf{u}$.

3.4. Governing equations in bulk fluids

At this step, we easily obtain the evolution equations by the energy dissipation in bulk fluid. Taking the Cahn-Hilliard type of material conservation equation with NaSt Eqs. (3.6), the Cahn-Hilliard-Navier-Stokes model (CHNS), or the so-called model H, is derived,

$$\begin{aligned} \nabla \cdot \mathbf{u} &= 0, \\ \partial c_i / \partial t + \mathbf{u} \cdot \nabla c_i &= \nabla \cdot (\mathcal{M} \nabla \mu_i), \\ \rho d\mathbf{u}/dt &= -\nabla p - \sum_i c_i \nabla \mu_i + \nabla \cdot [\eta (\nabla \mathbf{u} + \nabla \mathbf{u}^T)], \end{aligned} \quad (3.8)$$

in which the bulk chemical potential is defined, with $\mu_i = \partial f / \partial c_i - \kappa \nabla^2 c_i$. The mobility \mathcal{M} scales the bulk diffusion which follows the Onsager's relation; more details in our previous work Zhang *et al.* (2021).

3.5. Governing equations in LAL

As the chemical free energy fluctuation in LAL can be dissipated via the surface diffusion (Yue *et al.* 2010); see Eq. (3.2), we may question: (I) Why the diffusion process cannot lead to fluid flow in LAL? (II) If the unmovable molecules in LAL obey the mathematical no-slip boundary condition, what is the physical origin of it? (III) Is there a possible kinetic energy dissipation inside LAL which may violate the no-slip boundary condition?

To answer these crucial questions, we “forget” the no-slip boundary condition, and focus on deducing the feasible force balance equation in LAL. Still, the skeleton key is the total energy minimization. Adding Eqs. (3.2), (3.3) (3.7), the total energy functional \mathcal{L} decay as

$$\begin{aligned} \frac{d\mathcal{L}}{dt} = & \int_{\Omega} \left[\sum_i \left(\frac{\partial f}{\partial c_i} - \kappa \nabla^2 c_i \right) \frac{dc_i}{dt} - \underline{\mathbf{T}} : \nabla \mathbf{u} \right] d\Omega - \int_{\partial\Omega} \left[\sum_i (\kappa \nabla \bar{c}_i \cdot \mathbf{n}) \frac{d\bar{c}_i}{dt} + \underline{\mathbf{T}} \cdot \mathbf{n} \cdot \bar{\mathbf{u}} \right] dL \\ & + \int_L \left[\sum_i \left(\frac{\partial f_w}{\partial \bar{c}_i} - \kappa' \nabla_s^2 \bar{c}_i \right) \frac{d\bar{c}_i}{dt} + \sum_i \nabla_s \cdot (\kappa' \nabla_s \bar{c}_i \otimes \nabla_s \bar{c}_i) \cdot \bar{\mathbf{u}} + \left(\nabla_s \bar{p} + \rho \frac{d\bar{\mathbf{u}}}{dt} \right) \cdot \bar{\mathbf{u}} \right] \delta l dL. \end{aligned} \quad (3.9)$$

Substituting CHNS into Eq. (3.9), we have

$$\begin{aligned} \frac{d\mathcal{L}}{dt} = & - \int_{\Omega} \left[\sum_i \mathcal{M} (\nabla \mu_i)^2 + \eta \nabla \mathbf{u} : \nabla \mathbf{u} \right] d\Omega + \int_L \left[\sum_i \left(\frac{\partial f_w}{\partial \bar{c}_i} - \kappa \nabla \bar{c}_i \cdot \mathbf{n} / \delta l - \kappa' \nabla_s^2 \bar{c}_i \right) \frac{d\bar{c}_i}{dt} \right] \delta l dL \\ & + \int_L \left[\sum_i \nabla_s \cdot (\kappa' \nabla_s \bar{c}_i \otimes \nabla_s \bar{c}_i) + \nabla_s \bar{p} - \underline{\mathbf{T}} \cdot \mathbf{n} \cdot \bar{\mathbf{u}} / \delta l + \rho \frac{d\bar{\mathbf{u}}}{dt} \right] \cdot \bar{\mathbf{u}} \delta l dL. \end{aligned} \quad (3.10)$$

3.5.1. Composition evolution equation in LAL

Inside Langmuir adsorption layer, we collect all terms with the total derivative $d\bar{c}_i/dt$ and obtain the composition evolution equation,

$$\partial \bar{c}_i / \partial t + \bar{\mathbf{u}} \cdot \nabla_s \bar{c}_i = \Gamma \nabla_s^2 \bar{\mu}_i, \quad (3.11)$$

in which the surface mobility Γ scales the energy dissipation in LAL via surface diffusion process. Particularly, we define the chemical potential in LAL,

$$\bar{\mu}_i = \partial f_w / \partial \bar{c}_i - \kappa \nabla_n \bar{c}_i / \delta l - \kappa' \nabla_s^2 \bar{c}_i, \quad (3.12)$$

with $\nabla_n \bar{c}_i := \nabla \bar{c}_i \cdot \mathbf{n}$. Noteworthy, the second term in Eq. (3.12) stems from the last integral of Eq. (3.1), denoting the thermodynamic coupling of fluids in both bulk and LAL.

Different from previous approaches (Yue *et al.* 2004; Jacqmin 2000) where the surface chemical potential $\bar{\mu}_i$ is introduced as a pure mathematic concept with the unit of J/m^2 , the chemical potential in the present LAL approach now has a clear physical meaning which is related to the interacting solid and fluid molecules and has the unit of J/m^3 .

3.5.2. Force balance equation in LAL

Then, when the slip velocity $\bar{\mathbf{u}}$ in LAL exists, it modifies the kinetic energy dissipation. Gathering all terms containing $\bar{\mathbf{u}}$, the force balance in LAL becomes

$$\begin{aligned} \nabla_s \cdot \bar{\mathbf{u}} &= 0, \\ \rho \frac{d\bar{\mathbf{u}}}{dt} &= \bar{\mathbf{f}} + \mathbf{F}_v + \mathbf{F}, \end{aligned} \quad (3.13)$$

in which the force $\bar{\mathbf{f}} = -\nabla_s \cdot (\bar{\mathbf{P}}\mathbf{I} + \bar{\mathbf{\Theta}})$ is derived by the divergence of the stress tensors, with the grand potential \bar{P} , and the thermodynamic stress tensor $\bar{\mathbf{\Theta}}$ taking

$$\bar{P} = \bar{p} - g_w + \sum_i (\delta g_w / \delta \bar{c}_i) \bar{c}_i, \quad \bar{\mathbf{\Theta}} = -[g_w - \sum_i (\delta g_w / \delta \bar{c}_i) \bar{c}_i] \mathbf{I} + \sum_i \kappa' \nabla_s \bar{c}_i \otimes \nabla_s \bar{c}_i.$$

However, the rest two forces in Eq. (3.13) are not stemmed from any conservative vector fields. (I) Distinct from the bulk fluid, the fluid viscous force is composed of two aspects,

$$\mathbf{F}_v = \nabla_s \cdot \bar{\mathbf{T}} + \underline{\mathbf{T}} \cdot \mathbf{n} / \delta l = \nabla_s \cdot [\eta (\nabla_s \bar{\mathbf{u}} + \nabla_s \bar{\mathbf{u}}^T)] + \eta (\nabla_n \bar{\mathbf{u}} + \nabla_n \bar{\mathbf{u}}^T) / \delta l.$$

The first term $\nabla_s \cdot \eta (\nabla_s \bar{\mathbf{u}} + \nabla_s \bar{\mathbf{u}}^T)$ describes the viscous stress of molecular interactions within the fluid amid LAL. The second term $\eta (\nabla_n \bar{\mathbf{u}} + \nabla_n \bar{\mathbf{u}}^T) / \delta l$ measures the viscous friction of bulk fluid molecules onto LAL and is emanated from the second integral in Eq. (3.7), which highlights the hydrodynamic coupling of fluids in both bulk and LAL. Since the fluid velocity component in substrate normal direction of LAL is 0, we write the viscous force as

$$\mathbf{F}_v = \nabla \cdot [\eta (\nabla \bar{\mathbf{u}} + \nabla \bar{\mathbf{u}}^T)].$$

(II) Besides the interactions between fluid molecules, the force balance equation in LAL contains friction force \mathbf{F} which is emanated from the relative tangential motion of fluid-solid molecules. In this work, we apply Navier's interfacial constitutive relation (Navier 1822) of \mathbf{F} with the slip velocity $\bar{\mathbf{u}}_s = \bar{\mathbf{u}} - \mathbf{u}_w$ relative to the solid substrate velocity \mathbf{u}_w ,

$$\mathbf{F} = -\lambda \bar{\mathbf{u}}_s.$$

This relation can also be derived with Mori-Zwanzig formalism (Mori 1965; Zwanzig 1961); see Bocquet & Barrat (1994); Bui & Cox (2024) for more details. For the sake of brevity, the solid-fluid friction is scaled by the isotropic friction coefficient λ . More analyses on the friction force will be discussed later in Sec. 4.

Finally, we deduce the complete governing equations in LAL,

$$\begin{aligned} \nabla_s \cdot \bar{\mathbf{u}} &= 0, \\ \partial \bar{c}_i / \partial t + \bar{\mathbf{u}} \cdot \nabla_s \bar{c}_i &= \Gamma \nabla_s^2 \bar{\mu}_i, \\ \rho \, d\bar{\mathbf{u}} / dt &= -\nabla_s \bar{p} - \sum_i \bar{c}_i \nabla_s \bar{\mu}_i + \nabla \cdot [\eta (\nabla \bar{\mathbf{u}} + \nabla \bar{\mathbf{u}}^T)] - \lambda \bar{\mathbf{u}}_s. \end{aligned} \quad (3.14)$$

3.6. Total energy functional dissipation

Proof. Substituting the evolution equations Eqs. (3.14) into Eq. (3.10), the total energy functional of the *multicomponent fluid* dissipates with time as,

$$d\mathcal{L} / dt = -\int_{\Omega} [\sum_i \mathcal{M}(\nabla \mu_i)^2 + \eta \nabla \mathbf{u} : \nabla \mathbf{u}] \, d\Omega - \int_L [\sum_i \Gamma (\nabla_s \bar{\mu}_i)^2 + \eta \nabla \bar{\mathbf{u}} : \nabla \bar{\mathbf{u}} + \lambda \bar{\mathbf{u}}_s \cdot \bar{\mathbf{u}}] \, \delta l \, dL.$$

Noting that the friction force $\mathbf{F} = -\lambda \bar{\mathbf{u}}_s$ can either accelerate, or decelerate the fluid, we shall not forget the power made by the solid-fluid friction onto the *solid substrate*, namely

$$d\mathcal{K}_w / dt = \int_L -\mathbf{F} \cdot \mathbf{u}_w \, \delta l \, dL = \int_L \lambda \bar{\mathbf{u}}_s \cdot \mathbf{u}_w \, \delta l \, dL.$$

Combining $d\mathcal{L} / dt$ with $d\mathcal{K}_w / dt$, the total energy functional of the *multicomponent fluid and solid substrate* dissipates with time as,

$$\frac{d\mathcal{L}_T}{dt} = -\int_{\Omega} [\sum_i \mathcal{M}(\nabla \mu_i)^2 + \eta \nabla \mathbf{u} : \nabla \mathbf{u}] \, d\Omega - \int_L [\sum_i \Gamma (\nabla_s \bar{\mu}_i)^2 + \eta \nabla \bar{\mathbf{u}} : \nabla \bar{\mathbf{u}} + \lambda \bar{\mathbf{u}}_s^2] \, \delta l \, dL \leq 0 \quad \blacksquare$$

The first integral in domain Ω denotes the energy dissipation in bulk fluids via diffusion and fluid viscous effect. The second integral in LAL highlights the three feasible energy

minimizing mechanisms, namely, the surface diffusion (depletion/adsorption), the fluid viscous effect, and the solid-fluid friction.

4. Physical origin of solid-fluid friction

Before heeding the influence of friction on fluid flow, we need to have a clear definition for the solid-fluid friction which is vaguely defined in Sec. 3.5.2. Every force appearing in the force balance equation of LAL is derived from the minimization of the corresponding energy, except for the friction force \mathbf{F} . Just like other previous studies, we simply introduce this force and accept it without further justification. Given that the fluctuation-dissipation theorem is a universal principle for materials across scales from galaxies to quantum systems, how can friction forces lack a corresponding energy? What is the energy term associated with friction? What microscopic factors influence the magnitude of friction?

4.1. Green-Kubo relation

A common method to extract the friction magnitude is through molecular dynamics (MD) simulations, based on the theory introduced by Bocquet & Barrat (1994). Here, the linear response is assumed to hold under weak fluid flow conditions. As derived from the energy law in Sec. 3.5.2, the friction force $\mathbf{F}(\mathbf{x}, t)$ alters the fluid momentum, leading to dissipation that follows the Green-Kubo relation at equilibrium,

$$\lambda_{\text{G-K}} = 1/(Ak_B T) \int_0^\infty dt \langle \mathbf{F}(\mathbf{x}, t), \mathbf{F}(\mathbf{x}, 0) \rangle, \quad (4.1)$$

with the friction area denoted by A . If the bulk fluid flow is negligible, the friction coefficient $\lambda_{\text{G-K}}$ tells an intrinsic property of the solid-fluid interface. However, as noted by Bui & Cox (2024), the energy dissipation of the bulk fluid due to viscous stress also contributes to the calculation of Eq. (4.1) in MD simulations, corresponding to the hydrodynamic coupling of bulk and LAL by the second integral in Eq. (3.7). They argue that the Green-Kubo relation only accounts for the combined effects of solid-liquid intermolecular friction and fluid viscous effect.

To eliminate the influence of bulk fluids, they introduced the so-called effective friction coefficient λ_{eff} , which cancels the influence of the bulk liquid flow profile. Consequently, λ_{eff} incorporates a geometry correction related to the simulation setup. For example, for Poiseuille flow in a cylindrical pipe, λ_{eff} decays with the pipe radius. In 2D Poiseuille flow between parallel planes, λ_{eff} is inversely related to the plane spacing. Hence, their studies affirm that friction at the solid-fluid interface is not purely an intrinsic property of the substrate, but also depends on the flow setup geometry.

To explain the concept of the effective friction coefficient, we formulate the Langevin equation for the force balance in LAL inside one dimensional Poiseuille flow ($\bar{u}_s = \bar{u}$),

$$\rho d\bar{u}/dt = -\partial_x \bar{p} + \eta \partial_n \bar{u} / \delta l - \lambda \bar{u} + \tilde{\xi}.$$

The pressure gradient $\partial_x \bar{p}$ and thermal noise $\tilde{\xi}$ propels the flow, while other two dissipative terms counteract the fluid momentum: the friction $-\lambda \bar{u}$ arises from the intrinsic property of the solid-liquid interactions; the viscous stress $\eta \partial_n \bar{u}$ describes the drag force exerted by the bulk fluid on the material in LAL, which is only the intrinsic property of fluid itself. The Green-Kubo relation therefore describes the equilibrium of the Langevin equation where the fluctuation-dissipation in LAL is coupled with the bulk fluid above it. Therefore, when the flow setup geometry changes, the velocity profile of the bulk fluid varies accordingly. As a result, the viscous stress $\eta \partial_n \bar{u}$ will be modified, altering the steady-state of \bar{u} in LAL.

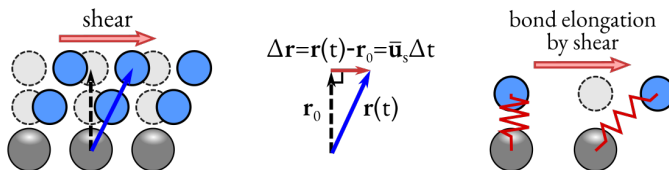


Figure 3: Shear deformation pushes fluid molecules (blue circles) away from equilibrium positions (dashed circles) along the tangential direction of the solid surface (gray). The displacement $\Delta \mathbf{r} = \bar{\mathbf{u}}_s \Delta t$ varies linearly with the slip velocity $\bar{\mathbf{u}}_s$.

Consequently, the friction coefficient λ_{G-K} obtained via the Green-Kubo relation certainly absorbs the impact of geometry-dependent bulk fluid flow and cannot represent the pure property of fluid-solid friction.

4.2. Molecule perspective

Now, we provide our understanding of the physical origin of solid-fluid friction from a molecular perspective and attempt to derive an expression for the intrinsic friction coefficient. Initially, we temporarily name the total solid-fluid interaction energy within the LAL as

$$\mathcal{E} = \int_{\mathbf{L}} f_w(\bar{\mathbf{c}}, \mathbf{r}) \delta l \, dL.$$

Here, $\mathbf{r}(t)$ represents the spacing between the fluid and solid molecules; see figure 3. Under small fluctuations, such as minor shear deformations, the fluid molecules move away from their equilibrium position, the energy density can be expanded as a Taylor series in terms of displacement $\Delta \mathbf{r} = \bar{\mathbf{u}}_s \Delta t$ (Cai *et al.* 2024) as,

$$f_w(\bar{\mathbf{c}}, \mathbf{r}_0 \pm \Delta \mathbf{r}) = f_w(\bar{\mathbf{c}}, \mathbf{r}_0) + \frac{\partial^2 f_w / \partial \Delta \mathbf{r}^2}{2} (\bar{\mathbf{u}}_s \Delta t)^2 + O(\bar{\mathbf{u}}_s^4 \Delta t^4),$$

where Δt denotes the characteristic timescale of shear deformation. Hence, the power of the friction is expressed $\mathbf{F} \cdot \bar{\mathbf{u}}_s = -df_w/dt$ which gives rise to the average friction force, $\mathbf{F} = -(\partial^2 f_w / \partial \Delta \mathbf{r}^2) \bar{\mathbf{u}}_s \Delta t = -\lambda \bar{\mathbf{u}}_s$, so that the friction coefficient is written as

$$\lambda(\bar{\mathbf{c}}) = (\partial^2 f_w / \partial \Delta \mathbf{r}^2) \Delta t.$$

It is noteworthy that the displacement $\Delta \mathbf{r}$ denotes the elongation of solid-fluid bond which is depicted by the red spring-like structure in figure 3, representing the physical model of the fluid-solid bond (Shimizu *et al.* 1998). Thus, the scaling parameter $\partial^2 f_w / \partial \Delta \mathbf{r}^2$ is determined by the magnitudes of the solid-fluid bonding energy. Due to this reason, the average friction force \mathbf{F} takes a formulation analogous to Hooke's law, acting as the counter force to stop the relative motion of molecules and bring them back to their equilibrium position.

Resulting from this, we suggest that the fluid-solid friction indicates another dissipation mechanism for the wall energy fluctuations. Conventional theories mainly focus on the dissipation by composition changes via (I) depletion/adsorption and (II) surface diffusion. Both account for the variance of f_w with respect to the composition \bar{c}_i . (III) Fluid flow induced by Korteweg stress and Maxwell stress amid the fluid phase, dissipates through fluid intermolecular friction (viscous stress) (Zhang *et al.* 2024b).

In this work, we highlight a fourth mechanism that is often overlooked. (IV) Fluid flow induces relative motion between solid-fluid molecules at the interface, causing variations in bond length and angle. These molecular deformations alter the corresponding energy landscape, generating a restorative force that pulls fluid molecules back toward their equilibrium positions, thereby resisting their departure. This resistance is the fundamental

source of solid-fluid intermolecular friction. Since the friction force is associated with bond rotation/elongation, it can neither be neglected nor assigned arbitrary magnitudes. Moreover, we emphasize that both the friction force and the depletion/adsorption force originate from the same fundamental mechanism, namely, the minimization of wall energy at the atomic scale. The key distinction between them lies in their relation to molecular motion: friction force pertains to shear motion, governed by hydrodynamic interactions, while depletion/adsorption force arises from diffusive motion, driven by thermodynamic effects. This distinction may help explain why some frying pans are coated with PTFE (polytetrafluoroethylene). The fluorocarbon compounds exhibit weak van der Waals interactions due to the low electric polarizability of fluorine, resulting in two valuable properties: hydrophobicity (low adsorption) and slippery (low friction).

5. Steady state in boundary layer

This section focuses on the steady-state behavior of the material in LAL, considering energy dissipation through (I) diffusion and (II) convection. Using the pre-defined governing equations in Sec. 3, we emphasize their consistency with the previously established wetting boundary condition (Qian *et al.* 2006; Yue *et al.* 2010; Wang *et al.* 2023). Specifically, the physical interpretation of the mathematical approaches will be clarified.

5.1. Chemical equilibrium in LAL and Young's law

First, we demonstrate the thermodynamic equilibrium and show that our wetting boundary model is thermodynamically consistent with sharp interface models. By multiplying the LAL chemical potential Eq. (3.12) with δl ,

$$\bar{\mu}_i \delta l = \partial \gamma / \partial \bar{c}_i - \kappa \nabla_n \bar{c}_i - \kappa' \nabla_s^2 \bar{c}_i \delta l, \quad (5.1)$$

where $\gamma = \int_{\bar{c}_0}^{\bar{c}_\infty} \bar{\mu}_i \delta l d\bar{c}_i$. As illustrated by the sessile droplet in figure 1, integrating Eq. (5.1) from the equilibrium liquid composition \bar{c}_0 at the droplet center ($r = 0$) to the equilibrium air composition \bar{c}_∞ at $r = \infty$, yields

$$\begin{aligned} \int_{\bar{c}_0}^{\bar{c}_\infty} \bar{\mu}_i \delta l d\bar{c}_i &= \gamma(\bar{c}_\infty) - \gamma(\bar{c}_0) - \int_{\bar{c}_0}^{\bar{c}_\infty} \left[\kappa \frac{\partial c_i}{\partial R} \cos \theta + \frac{\kappa'}{r} \frac{\partial}{\partial r} \left(r \frac{\partial \bar{c}_i}{\partial r} \right) \delta l \right] d\bar{c}_i \\ &= \Delta \gamma - \sigma_{LV} \cos \theta - \int_0^\infty \frac{\kappa'}{r} \left(\frac{\partial \bar{c}_i}{\partial r} \right)^2 \delta l dr \\ &= \Delta \gamma - \sigma_{LV} \cos \theta - \frac{\tau \delta l}{r_c}, \end{aligned} \quad (5.2)$$

in which the droplet-air interfacial tension is expressed by $\sigma_{LV} := \int_0^\infty \kappa (\partial_R c_i)^2 dR$, and R guiding the droplet surface normal direction. The solid-liquid and solid-air interfacial tensions are denoted by $\gamma(\bar{c}_0)$ and $\gamma(\bar{c}_\infty)$, respectively. In addition, r_c represents the contact line radius. More details on the line tension parameter, $\tau := \int_0^\infty \kappa' (\partial_r \bar{c}_i)^2 dr$, can be found in our previous work (Zhang *et al.* 2023).

Setting Eq. (5.2) equal to 0, the Young's law with the line tension effect (Amirfazli & Neumann 2004; Law *et al.* 2017) is recovered,

$$\cos \theta = \cos \theta_Y - \frac{\tau / \sigma_{LV}}{r_c} \delta l + O(r_c^{-2}), \quad (5.3)$$

where $\theta_Y = \arccos(\Delta \gamma / \sigma_{LV})$ represents the Young's angle without line tension. Notably, Eq. (5.3) provides a different perspective on the physical meaning of the LAL thickness, δl . In Sec. 2.1.2, we defined the LAL as the range of solid-fluid interactions. Thus, at

distances larger than δl into the bulk fluid bulk, molecules are influenced solely by fluid molecular interactions, with no solid-fluid interaction. As a result, the LAL and bulk fluid are intrinsically separated by the fictitious surface located at the distance δl above the substrate. Based on this understanding, we propose that this fictitious plane separating the LAL from the bulk fluid at δl is equivalent to the Gibbs dividing surface (Gibbs 1928; Schimmele *et al.* 2007). Hence, δl scales the magnitude of the line tension, consistent with previous studies (Wang & Nestler 2024b; Zhang *et al.* 2023; Schimmele *et al.* 2007).

5.2. Steady fluid field in LAL

Next, we focus on the steady state of the *binary* fluid flow in LAL, when $\rho d\bar{\mathbf{u}}/dt = 0$. The composition of fluid one is denoted as \bar{c} , so that the second composition is $1 - \bar{c}$. Without loss of generality, we simplify the fluid flow to the 2-dimensional case and express the force balance in the x-o-n coordinate system, where x and n represent the tangential and normal directions of the substrate, respectively. In x-direction, the force balance is given by:

$$-\partial_x \bar{p} - \bar{c} \partial_x \bar{\mu} + \partial_x (\eta \partial_x \bar{u}) + (\eta/\delta l) \partial_n \bar{u} - \lambda \bar{u}_s = 0. \quad (5.4)$$

5.2.1. Generalized Navier boundary condition

If no pressure gradient is applied in the x-direction, as in Couette flow and droplet wetting, we have $\partial_x \bar{p} = 0$, and we multiply both sides of Eq. (5.4) by δl ,

$$(\lambda \delta l) \bar{u}_s = -c^s \partial_x \bar{\mu} + \eta \partial_n \bar{u} + \delta l \partial_x (\eta \partial_x \bar{u}), \quad (5.5)$$

where $c^s = \bar{c} \delta l$ represents the fluid surface composition. Eq. (5.5) bears a clear resemblance to the generalized Navier boundary condition (GNBC) presented in the classic paper by Qian *et al.* (2006), with

$$\beta_n \bar{u}_s = -c^s \partial_x \bar{\mu} + \eta (\partial_n \bar{u} + \partial_x \bar{v}). \quad (5.6)$$

The friction coefficient $\lambda = \beta_n/\delta l$ is related to the slip coefficient β_n defined by Navier. In addition to these similarities, our Eq. (5.5) also introduces two distinctions:

- The normal stress term $\partial_x (\eta \partial_x \bar{u})$ vanishes in GNBC. For single-phase flow, this term is always zero. However, in multiphase flow with an interface, differences in velocity and viscosity between phases contribute an additional viscous force term that cannot be neglected. The vanishing of this term is due to the application of the divergence theorem in the derivation of Eq. (5.6), where the volumetric functional variation over the entire domain is automatically transformed into surface normal flux. Implicitly, the energy functional variation in the boundary tangential direction is neglected. Although this tangential functional variation does not affect the total energy flux *through* the domain boundary, it can alter the boundary energy functional density and, consequently, influence the local momentum and composition distributions at the boundaries.

- Our equation does not contain $\eta \partial_x \bar{v}$, being consistent with Navier boundary condition.

5.2.2. Navier boundary condition

For the single phase flow at the steady state, the unbalanced thermodynamic force related to inhomogeneous composition \bar{c} is neglected, Eq. (5.5) becomes

$$(\lambda \delta l) \bar{u}_s = \eta \partial_n \bar{u} + \delta l \partial_x (\eta \partial_x \bar{u}).$$

Considering the flow where the velocity in the n-direction is absent, i.e., $\partial_n \bar{v} = 0$, such as in Couette and Poiseuille flows, the normal component of the viscous stress $\eta \partial_x \bar{u} = 0$, leads to

the Navier boundary condition (NBC) with the so-called Navier slip length is derived as

$$l_s = \frac{\eta}{\lambda \delta l}. \quad (5.7)$$

Moreover, when the friction force dominates with the coefficient $\lambda \rightarrow \infty$, the Navier slip length $l_s = 0$ recovers the no-slip boundary condition.

Noteworthy, we argue that the Navier slip length l_s is merely a fictitious parameter without the clear physical definition. This concept is introduced because Navier-Stokes equation is a second-order PDE that requires a corresponding mathematical boundary condition for the solution. To elucidate the physical interpretation of slip length l_s , we may consider the energy dissipation of the single phase flow ($d\mathcal{F}/dt = 0$) and easily find that

$$d\mathcal{L}_T/dt = \int_{\partial\Omega} (-\underline{\bar{\mathbf{T}}} \cdot \underline{\bar{\mathbf{u}}} \cdot \mathbf{n} + \mathbf{F} \cdot \mathbf{u}_w \delta l) dL - \int_{\Omega} \eta \nabla \mathbf{u} : \nabla \mathbf{u} d\Omega, \quad (5.8)$$

in which the first and second integrals represent the viscous dissipation at the boundary $\partial\Omega$ and in the bulk Ω , respectively. Usually, two mathematical approaches on the domain boundary $\partial\Omega$ ensure the total energy decay over time, namely,

- *no-slip boundary condition* (BC) with $\underline{\bar{\mathbf{u}}} = \mathbf{0}$ and $\mathbf{F} = \mathbf{0}$ gives rise to

$$d\mathcal{L}_T/dt = - \int_{\Omega} \eta \nabla \mathbf{u} : \nabla \mathbf{u} d\Omega \leq 0,$$

indicating the energy can only be dissipated by the bulk fluid. The solid-fluid boundary does not dissipate any energy.

- *Navier boundary condition* (NBC) with $l_s \partial_n \underline{\bar{\mathbf{u}}} = \underline{\bar{\mathbf{u}}}_s$ and $\mathbf{F} = -(\eta/l_s) \underline{\bar{\mathbf{u}}}_s$ result in

$$d\mathcal{L}_T/dt = - \int_{\partial\Omega} (\eta/l_s) \underline{\bar{\mathbf{u}}}_s^2 dL - \int_{\Omega} \eta \nabla \mathbf{u} : \nabla \mathbf{u} d\Omega \leq 0.$$

In this case, the kinetic energy dissipation on the solid-fluid boundary $\partial\Omega$ also plays a role. With the increase in the slip length l_s , the dissipation on the boundary becomes weaker. Still, for a given system, the value of l_s is unknown and should be obtained by other indirect methods, such as MD simulation.

But the no-slip BC and NBC are not the only two conditions that guarantee the energy minimization. Based on the above discussion, we suggest that the no-slip BC, NBC, and GNBC are merely potential strong constraints equivalent to the steady states of our force balance equation Eq. (3.14) in LAL with $d\underline{\bar{\mathbf{u}}}/dt = 0$. In fact, neither the slip velocity $\underline{\bar{\mathbf{u}}}_s$, nor the slip length l_s , should be assigned by the constant values before reaching the steady state. In other words, the fluid flow in the LAL should develop itself. Initially, the fluid material in LAL undergoes an acceleration process, beginning to move along the substrate surface with $d\underline{\bar{\mathbf{u}}}/dt > 0$. For instance, in Couette flow, the initial speed-up results from the solid-fluid friction force \mathbf{F} . In Poiseuille flow, it originates from the pressure gradient $-\nabla p$. And in droplet wetting, the impulse arises from the unbalanced thermodynamic force $-\bar{c} \nabla \bar{\mu}$. The materials then gradually slow down, as other forces come into play to dissipate the kinetic energy. Eventually, the fluid molecules reach the force balance and keep the constant slip velocity $\underline{\bar{\mathbf{u}}}_s$ at steady states.

Besides, during the development of the slip velocity, the velocity gradient $\partial_n \underline{\bar{\mathbf{u}}}$ in the LAL will also vary with time. Therefore, we suggest that the pre-defined constant Navier slip length l_s in Eq. (5.7) may be physically plausible. Even for the MD simulation with Green-Kubo relation, only l_s at equilibrium is obtained. If l_s is merely a mathematical tool invented to solve the second-order PDE, why couldn't we put it aside and use other more generalized ways to define the slip phenomenon in a more physical manner? In the following section, we will show that the solid-fluid friction is of great importance for the slip phenomenon.

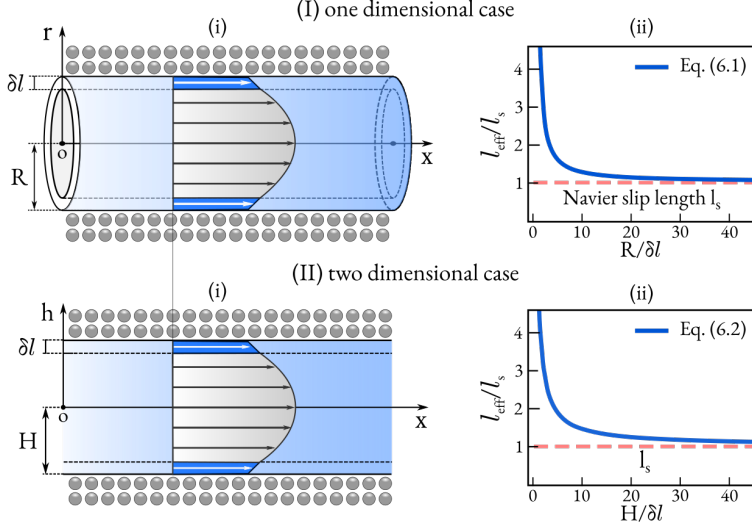


Figure 4: (I) 1D Poiseuille flow through a tube with radius R . (i) Geometry. (ii) Effective slip length l_{eff} decays with R to Navier slip length l_s for $R \rightarrow \infty$. (II) 2D Poiseuille flow between two planes with spacing H . (i) Geometry. (ii) l_{eff} converges to l_s for $H \rightarrow \infty$.

6. Case study

In this section, we apply our slip model to several conventional flow configurations, and select the thickness of the Langmuir adsorption layer (LAL) as the characteristic length scale, setting $\delta l = 1$. To emphasize the roles of surface tension and viscous stress in microdroplets, we adopt water viscosity and water interfacial tension as characteristic values. Under these conditions, the system's Reynolds number remains $\text{Re} \ll 1$, indicating that fluid inertia is negligible. This enables us to further analyze the steady-state solutions of fluid motion with slip and friction, and compare our results to classical wetting theories, including Huh & Scriven and Cox & Voinov, for binary fluid systems. Since our study mainly focuses on theoretical modeling and analytical solutions, we do not incorporate numerical simulations in this work, as they cannot be directly compared to these classical theoretical frameworks.

6.1. Single phase flow

6.1.1. 1D Poiseuille flow

We start with the simplest single phase scenario and consider the one dimensional Poiseuille flow through the pipe with radius R . The velocity field is simplified in the cylindrical coordinates x - o - r , as demonstrated in figure 4(I)(i). The fluid velocity obeys the following force balances in the bulk fluid and LAL, as

$$\begin{cases} \nabla p = \eta \nabla^2 \mathbf{u}, & \text{in } r \in (-R + \delta l, R - \delta l), \\ \lambda \bar{u} = \eta \left(1 + \frac{\delta l}{r}\right) \frac{\partial \bar{u}}{\partial r} - \frac{dp}{dx}, & \text{in } r = \pm(R - \delta l). \end{cases}$$

The solution denotes the steady flow field related with the pipe radius as

$$\mathbf{u}(r) = \left[\frac{r^2 - (R - \delta l)^2}{4\eta} - \frac{R + 2\delta l}{2\lambda\delta l} \right] \frac{dp}{dx},$$

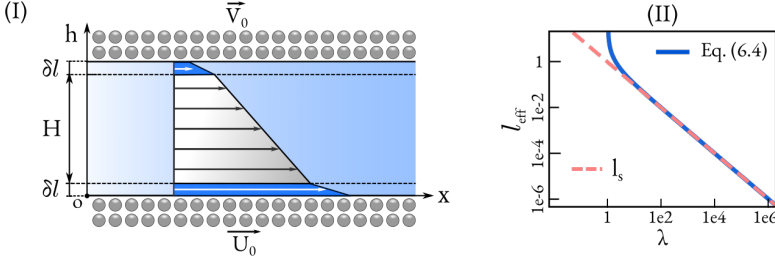


Figure 5: (I) Couette flow with the plane spacing $H + 2\delta l$. (II) Effective slip length l_{eff} decays with the increasing friction coefficient λ to the Navier slip length l_s at $\lambda \geq 20$.

which gives rise to the geometry dependent effective slip length on the pipe radius R ,

$$l_{\text{eff}} = \frac{R + 2\delta l}{R - \delta l} l_s. \quad (6.1)$$

For the large enough pipe with radius $R \gg \delta l$, l_{eff} approaches the Navier slip length l_s of Eq. (5.7) which shows no geometry dependence anymore.

6.1.2. 2D Poiseuille flow

Similarly, for the two dimensional Poiseuille flow through two parallel planes with spacing $2H$; see figure 4(II)(i), the fluid velocity field in x - h coordinates is described by the following force balance equation,

$$\begin{cases} \nabla p = \eta \nabla^2 \mathbf{u}, & \text{in } h \in (-H + \delta l, H - \delta l), \\ \lambda \bar{u} = \eta \partial \bar{u} / \partial h - dp/dx, & \text{in } h = \pm(H - \delta l), \end{cases}$$

which denotes the steady flow field as

$$u(h) = \left[\frac{h^2 - (H - \delta l)^2}{2\eta} - \frac{H}{\lambda \delta l} \right] \frac{dp}{dx},$$

leading to the geometry dependent effective slip length on the plane spacing $2H$ as

$$l_{\text{eff}} = \frac{H}{H - \delta l} l_s. \quad (6.2)$$

6.1.3. 2D Couette flow

For the 2 dimensional Couette flow between the parallel planes with spacing $H + 2\delta l$ illustrated in figure 5(I), the steady state obeys

$$\begin{cases} \mathbf{0} = \eta \nabla^2 \mathbf{u}, & \text{in } h \in (\delta l, H + \delta l), \\ \bar{u} - U_0 = l_s \partial \bar{u} / \partial h, & \text{in } h = \delta l / 2, \\ \bar{u} - V_0 = l_s \partial \bar{u} / \partial h, & \text{in } h = H + 3\delta l / 2. \end{cases}$$

On the upper plane with $h = H + 2\delta l$, the velocity boundary condition says $u = 0$, while at the lower plane $h = 0$, $u = U_0$. The steady fluid velocity inside the bulk reads is

$$u = kU_0 + (1 - kU_0)(h - H - \delta l)/H.$$

While in LAL of both planes, the steady velocities take

$$\bar{u} \Big|_{h=\delta l/2} = (1 - k)U_0, \quad \bar{u} \Big|_{h=H+3\delta l/2} = (1 - k)U_0. \quad (6.3)$$

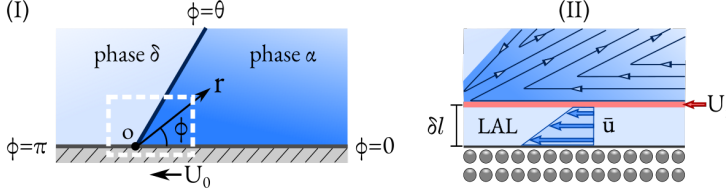


Figure 6: (I) Huh & Scriven wedge flow in the r - ϕ coordinates. $\alpha - \delta$ interface locates at $\phi = \theta$. The gray substrate moves to the left with the velocity U_0 . (II) The friction dissipation in LAL reduces the velocity at the red-colored boundary of LAL and bulk fluid with slip velocity $|U_1| < |U_0|$.

The parameter $k = \eta \delta l / [(\lambda \delta l^2 - \eta)(H + 2\delta l)]$ gives rise to the effective slip length,

$$l_{\text{eff}} = \frac{\eta}{\lambda \delta l - \eta / \delta l}. \quad (6.4)$$

Unlike Poiseuille flow, the effective slip length is unaffected by the plane spacing H . When the friction coefficient λ exceeds 20; see figure 5(II), l_{eff} converges to Navier slip length l_s .

All three cases above indicate that the slip length l_{eff} is not an intrinsic property of the solid-fluid interface, which is determined not only by fluid interaction in bulk fluids and the solid-fluid molecular forces in LAL but also by the flow setup. These simple case studies also indicate the plausible conclusion on the geometry dependent friction coefficient λ which is lacking concrete physical significance.

6.2. Huh & Scriven wedge flow

In next part, we discuss the more complex two phase fluids with slip boundary conditions.

6.2.1. Model

We adopt the classical Huh & Scriven theory to analyze the wedge flow inside both phases in the r - ϕ coordinates; see figure 6(I). The phases α and δ form the equilibrium contact angle θ , are defined by the region $\phi \in [0, \theta)$ and $\phi \in (\theta, \pi]$, respectively, while $\phi = \theta$ denotes the $\alpha - \delta$ interface. The stream function ψ of the wedge flow fulfills the bi-harmonic function,

$$\nabla^2 \nabla^2 \psi = 0. \quad (6.5)$$

Its general solution in the polar coordinate (r, ϕ) reads,

$$\begin{cases} \psi_\alpha = r(a \sin \phi + b \cos \phi + c \phi \sin \phi + d \phi \cos \phi), & \text{in phase } \alpha, \\ \psi_\delta = r(A \sin \phi + B \cos \phi + C \phi \sin \phi + D \phi \cos \phi), & \text{in phase } \delta. \end{cases} \quad (6.6)$$

The velocity components in each phase i ($i = \alpha, \delta$) are expressed as,

$$\mathbf{u}_r^i = -(1/r) \partial \psi_i / \partial \phi, \quad \mathbf{u}_\phi^i = \partial \psi_i / \partial r.$$

The eight unknown parameter in Eqs. (6.6) are calculated with the following boundary conditions. At the boundary of bulk liquid and LAL, no normal flow exists and the fluid in each phase only slips along the substrate tangential direction with,

$$\mathbf{u}_\phi^\alpha|_{\phi=0} = 0, \quad \mathbf{u}_\phi^\delta|_{\phi=\pi} = 0.$$

Meanwhile, at the fluid-fluid interface, the situation is similar. Fluid cannot move across its surface and the tangential velocity is identical in both phases, yielding

$$\mathbf{u}_r^\alpha|_{\phi=\theta} = \mathbf{u}_r^\delta|_{\phi=\theta}, \quad \mathbf{u}_\phi^\alpha|_{\phi=\theta} = 0, \quad \mathbf{u}_\phi^\delta|_{\phi=\theta} = 0.$$

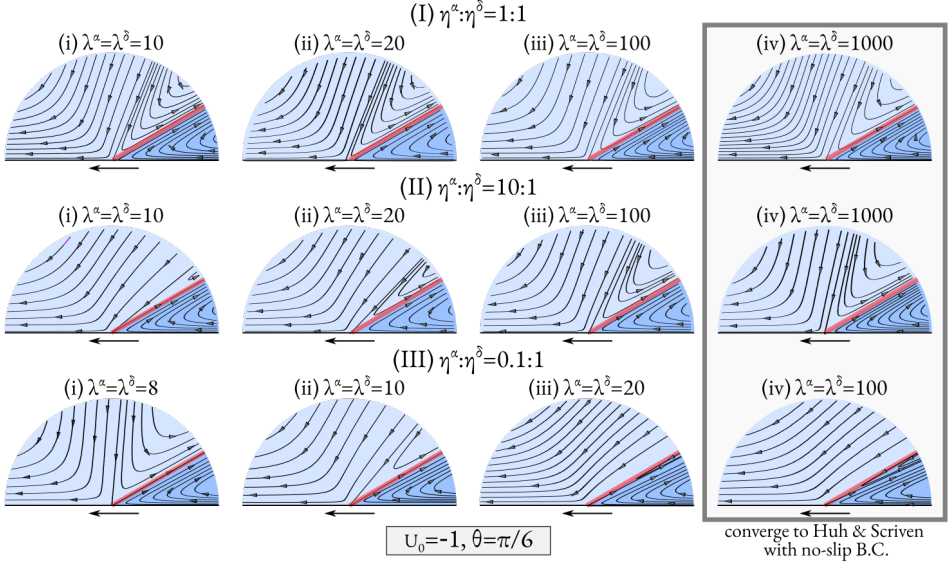


Figure 7: The streamlines of the wedge flow in phase α (mid blue) and δ (light blue) at the equilibrium contact angle $\theta = \pi/6$. The substrate shifts leftwards with the velocity $U_0 = -1$. (I) $\eta^\alpha:\eta^\delta = 1:1$; (II) $\eta^\alpha:\eta^\delta = 10:1$; (III) $\eta^\alpha:\eta^\delta = 0.1:1$. The friction coefficient $\lambda^\alpha = \lambda^\delta$ increase from left to right. The arrows show the velocity direction.

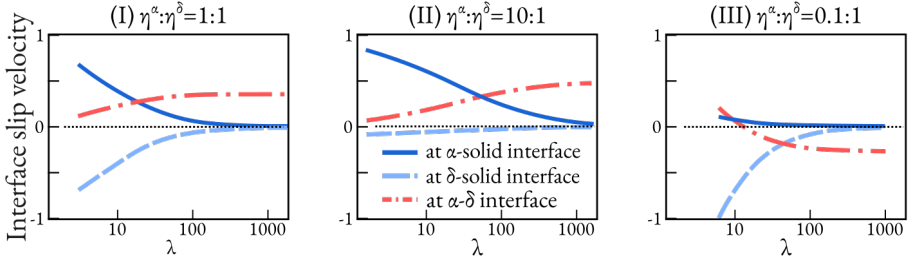


Figure 8: Three crucial slip velocities corresponding to the flow fields in figure 7, namely, the velocity of α - δ interface (red dotted-dash); $U_{\alpha s}$ at α -solid interface (blue dash); $U_{\delta s}$ at δ -solid interface (blue solid). (I) $\eta^\alpha:\eta^\delta = 1:1$; (II) $\eta^\alpha:\eta^\delta = 10:1$; (III) $\eta^\alpha:\eta^\delta = 0.1:1$.

The continuity of the tangential viscous stress at the $\alpha - \delta$ interface says

$$\eta^\alpha \partial^2 \psi_\alpha / \partial \phi^2 = \eta^\delta \partial^2 \psi_\delta / \partial \phi^2.$$

In contrast to the standard Huh & Scriven theory, we incorporate slip effects at the fluid-solid contact regions. Since friction magnitudes differ between the two phases, the corresponding slip velocities, $U_{\alpha s}$ and $U_{\delta s}$, follow distinct formulations,

$$\mathbf{u}_r^\alpha \Big|_{\phi=0} = U_{\alpha s}, \quad \mathbf{u}_r^\delta \Big|_{\phi=\pi} = U_{\delta s},$$

which could be obtained by the following force balance,

$$\lambda^\alpha (U_{\alpha s} - U_0) = \eta^\alpha \partial \mathbf{u}_r^\alpha / \partial \phi, \quad \lambda^\delta (U_0 - U_{\delta s}) = \eta^\delta \partial \mathbf{u}_r^\delta / \partial \phi, \quad (6.7)$$

with U_0 denotes the velocity of the substrate.

6.2.2. Flow pattern with slip boundary condition

Using the modified Huh & Scriven theory with slip boundary conditions, we computed the flow field within phases α and δ at the equilibrium contact angle $\theta = \pi/6$. The initial setup is illustrated in figure 7, where the substrate moves leftward at a velocity of $U_0 = -1$.

In the first setup in figure 7(I), both phases α (mid blue) and δ (light blue) are assigned with equal viscosity $\eta^\alpha = \eta^\delta$. The resulting streamlines exhibit a double-wedge flow pattern in phase δ and a single wedge in phase α . Regardless of changes in the friction coefficient $\lambda^{\alpha,\delta}$, the stream patterns remain consistent with the wedge flow predicted by the no-slip boundary condition. The only noticeable effect of increasing $\lambda^{\alpha,\delta}$ is a gradual reduction in slip velocity at both the α -solid and δ -solid interfaces, which ultimately approaches zero (no-slip) in figure 8(I).

In the second setup in figure 7(II), the viscosity of phase α is set to be 10 times larger than that of phase δ . When friction is strong ($\lambda^\alpha = \lambda^\delta = 1000$), the streamlines closely match the standard Huh & Scriven theory with no-slip boundary conditions, where the lower-viscosity phase δ shows a double-wedge flow pattern. However, as the friction force decreases (moving from the right to the left panel), the velocity damping within the LAL becomes increasingly significant. According to Eq. (6.7), the slip velocity in LAL follows a linear relationship with η/λ . Consequently, in the high-viscosity phase α , the substantial bulk viscous stress counteracts the material flow induced by friction, effectively dragging the LAL fluid and suppressing velocity transmission to phase δ . As a result, the velocity in phase α decreases, along with the interfacial velocity at the α - δ interface. Due to the coupled nature of the flow fields in both phases, the velocity reduction in α leads to modifications in δ , expanding the left flow wedge while compressing the mid-wedge region near the α - δ interface.

In the third setup in figure 7(III), the viscosity of phase δ becomes larger. According to standard Huh & Scriven no-slip flow, the double wedge pattern should emerge in the lower viscous phase α . However, when slip and friction are taken into account, the streamline patterns deviates greatly from the standard no-slip prediction. Only under strong friction conditions in figure 7(III)(iv) is the classical Huh & Scriven flow pattern recovered. As friction weakens, the double-wedge pattern gradually shifts into the high-viscosity phase δ , leaving the low viscosity phase α . The key mechanism behind this pattern shift lies in the interfacial velocity at the α - δ interface. Clearly shown in figure 8(III), the velocity at α - δ interface changes sign at $\lambda^\alpha = \lambda^\delta < 20$, aligning well with the flow pattern changes in figure 7(III)(ii) and (iii). These findings demonstrate that variations in friction within the LAL for different fluid phases can significantly influence the bulk flow field. Given that the physical origin of surface friction stems from wall energy (see Sec. 4.2), different materials exhibit distinct intermolecular bonding energies and van der Waals forces, resulting in different friction coefficients λ . Consequently, friction at the fluid-solid contact region can substantially alter the flow field and should not be overlooked in cases where the solid-fluid intermolecular bonding energy is weak relative to the fluid viscous stress.

6.3. Near triple junction

In the previous part, we discussed the wedge flow in two phase fluid $\alpha - \delta$ system induced by a moving substrate, focusing on the impact of slip in LAL on the flow field. Notably, conventional theories often neglect the force balance at the contact line region, where the Huh & Scriven paradox arises as $r \rightarrow 0$ approaching the triple junction. Qian *et al.* (2006) and Yue *et al.* (2010) addressed this issue in their simulations, demonstrating that the paradox does not actually arise in physical systems. This is because the real interface has a nano-scale thickness so that r does not approach zero. Building on their studies, we analyze the velocity field in the vicinity of the triple junction, with emphasis on the role of slip in the LAL.

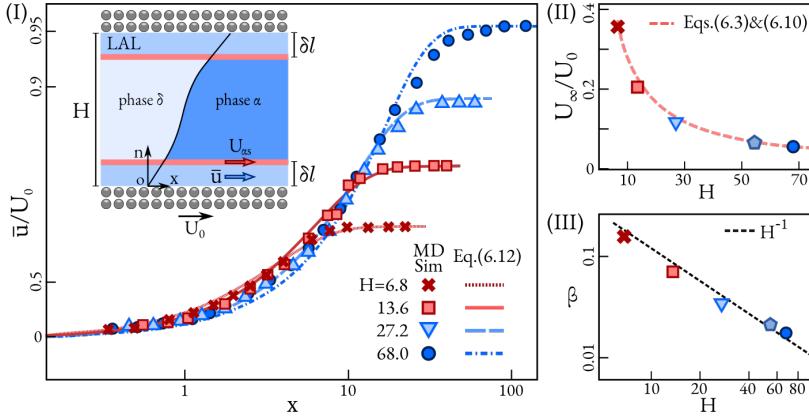


Figure 9: (I) Flow velocity \bar{u} in LAL from the triple junction $x = 0$. Open-colored symbols: \bar{u} by the molecular dynamic simulation in Qian *et al.* (2006). Colored curves: theory with Eq. (6.9). Inset: flow setup. (II) Far field flow velocity U_∞ in LAL fulfills Couette flow with both Eqs. (6.3) and (6.10). (III) The fitting parameter β shows the power law with the plane spacing H . The colored symbols in (II)(III) correspond to the markers in (I).

6.3.1. Velocity profile in LAL

With the setup in Qian *et al.* (2004, 2006); see the inset of figure 9(I), the flow velocity in the LAL shows a clear reduction near the triple junction region and becomes stagnated at the contact line position $x = 0$. It implies that the velocity in LAL is non-uniform which manifests the nonzero viscous term $\eta^\alpha \partial_{xx} \bar{u}$, and $\eta^\delta \partial_{xx} \bar{u}$. Particularly, in their study, equal viscosity is assigned for both phases, so that the velocity profile inside LAL becomes symmetric to $x = 0$. In this way, we rewrite the force balance equation in LAL Eq. (5.4) and focus on the phase α region with $x > 0$,

$$\eta^\alpha \partial_{xx} \bar{u} = \lambda^\alpha (\bar{u} - U_0) - \eta^\alpha \partial_n \bar{u}, \quad (6.8)$$

where we assume the balance of thermodynamic force $-c^s \partial_x \bar{\mu}$ with Laplace pressure $-\nabla \bar{p}$. At the position far away from the triple junction ($x \gg 1$), the viscous stress $\eta^\alpha \partial_{xx} \bar{u}$ becomes zero. Meanwhile, the far field is quasi Couette flow by which the velocity U_∞ is described by Eq. (6.3). In this way, the slip velocity $\bar{u}(x \rightarrow \infty) = U_\infty$ should be geometry dependent. Therefore, we replace the last term on the *rhs* of Eq. (6.8) by $\nu(U_{as} - \bar{u})$ in which U_{as} is the velocity in bulk fluid above LAL; see the red arrow in the inset of Fig. 9(I). ν is a scaling parameter which is fitted by the velocity profile via MD. As the bulk fluid flow follows the Huh & Scriven theory, U_{as} is treated as a constant, independent on x . After simplification, we have $\eta^\alpha \partial_{xx} \bar{u} = (\nu + \lambda^\alpha)(\bar{u} - U_\infty)$, whose solution reads

$$\bar{u} = (U_c - U_\infty) e^{-\beta x} + U_\infty, \quad (6.9)$$

in which the fitting parameter $\beta = \sqrt{(\nu + \lambda^\alpha)/\eta^\alpha}$ is also geometry dependent. Here, the zero contact line velocity $U_c = 0$ corresponds to the surface tension dominated scenario and is consistent with Huh & Scriven theory, as well as the MD simulations by Qian *et al.* (2006). In figure 9(I), we observe the exponential decay of the slip velocity with the position x away from the triple junction. The value of $\bar{u}(x)$ is extracted from Qian *et al.* (2006) and can be well described by our theoretical equation Eq. (6.8). By taking the droplet viscosity $\eta^\alpha = \eta^\delta = 2$,

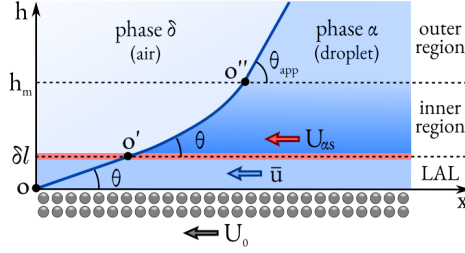


Figure 10: Droplet (phase α)-air (phase δ)-solid triple junction in the x - o - h coordinates follows the Cox-Voinov theory. The solid-liquid friction in the LAL and the fluid viscous force damp the fluid velocity at $h = \delta l$ as $|U_{0s}| < |U_0|$.

and the friction coefficient $\lambda^\alpha = \lambda^\delta = 1$, U_∞ in Eq. (6.3) is simplified as

$$U_\infty = U_0 \frac{2l_s}{H + 2l_s}, \quad (6.10)$$

which is demonstrated in figure 9(III). This indicates that the slip velocity at the far field follows the single phase Couette flow possessing the power law with the plane spacing reported by Qian *et al.* (2006). The only fitting parameter β shows the power law with the plane spacing H by the log-log plot in figure 9(III),

$$\beta \propto H^{-1} + \text{const.}$$

6.3.2. Cox-Voinov theory with slip

Based on the velocity analysis in LAL, we now heed the influence of the slip in LAL on the droplet wetting behavior, leveraging the classical Voinov theory (Voinov 1976; Cox 1986). As depicted in figure 10, the phase α , denoting the droplet phase, can be divided into three distinct regions: (I) outer region at $h > h_m$, the weak hydrodynamics is negligible, the $\alpha - \delta$ (droplet-air) interface forms the apparent contact angle θ_{app} with the flat substrate. (II) Inner region with $\delta l < h < h_m$, the fluid flow plays a crucial role, deforming the $\alpha - \delta$ interface (line $o'o''$), As a result, the local contact angle in the local contact angle θ deviates from θ_{app} . (III) Beneath the inner region, we highlight the Langmuir adsorption layer with the thickness δl . Given that $\delta l \ll h_m$, the $\alpha - \delta$ interface (line oo') in LAL is approximated as a straight line. According to the analysis in previous sections, the fluid flow within LAL is non-uniform, generating additional viscous stress on the droplet. Furthermore, the fluid-solid friction in LAL contributes an additional force balance in x -direction. Taking all these factors into account, we extend the standard Voinov theory to incorporate the effects of slip at the boundary. First, the force balance at the $\alpha - \delta$ (droplet-air) interface (line $o'o''$) of the inner region follows Moffatt (1964),

$$\sigma_{\text{LV}} \sin \theta \frac{d\theta}{dh} = \frac{\eta U_{0s}}{h} \frac{2 \sin^2 \theta}{\theta - \sin \theta \cos \theta}, \quad (6.11)$$

where the viscosity of phase α is denoted by η and the flow velocity at the bottom boundary of inner region (red solid line in figure 10) is U_{0s} . Integrating Eq. (6.11) on both side, the Voinov cubic relation works for any $\theta < 3\pi/4$,

$$\theta^3 = \theta_{\text{app}}^3 + \frac{9\eta U_{0s}}{\sigma_{\text{LV}}} \ln \left(\frac{h_m}{\delta l} \right). \quad (6.12)$$

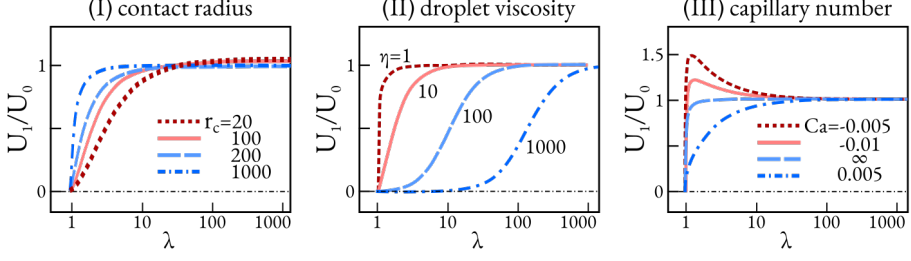


Figure 11: The flow velocity $U_{\alpha s}$ at the droplet-substrate interface reduction with the friction coefficient λ in LAL which is impacted by (I) droplet contact radius r_c ; (II) droplet viscosity η ; (III) capillary number Ca .

Noteworthy, in our consideration, the integral limit of Eq. (6.11) is not starting from $h = 0$, but $h = \delta l$ instead. Below the inner region, the force balance in LAL follows

$$\bar{c} \nabla \bar{\mu} = -\lambda(\bar{u} - U_0) + (\eta/\delta l)\partial_h \bar{u} + \eta \partial_{xx} \bar{u}.$$

Here, λ denotes the friction coefficient of phase α and solid substrate. Taking the exponential decay of fluid velocity in LAL based on Eq. (6.9); see figure 9(I),

$$\bar{u} = (U_c - U_\infty) \exp(-\beta x) + U_\infty,$$

where the relaxation parameter β is decided by both solid-fluid friction and fluid viscous drag and can be obtained by MD simulations. In this work, we use $\beta = 0.05$ fitted by data from the work of Qian *et al.* (2006), as shown in figure 9(III). The force balance in LAL yields the velocity at the α -solid interface

$$U_{\alpha s} = \frac{-2\sigma_{LV}(\cos \theta - \cos \theta_{app}) + (\lambda/\beta + \eta\beta)U_0 + \lambda U_0 r_c}{4\eta/(\lambda\beta) - \lambda/\beta - \eta\beta + \lambda r_c}. \quad (6.13)$$

When the α -solid friction coefficient $\lambda \rightarrow \infty$, $U_1 = U_0$ is equivalent to the no-slip boundary condition. Substituting Eq. (6.13) into Eq. (6.12), the Voinov cubic relation is influenced by the α -solid friction as

$$\theta^3 - \theta_{app}^3 = \frac{-2\sigma_{LV}(\cos \theta - \cos \theta_{app}) + (\lambda/\beta + \eta\beta)U_0 + \lambda U_0 r_c}{4\eta/(\lambda\beta) - \lambda/\beta - \eta\beta + \lambda r_c} \frac{9\eta}{\sigma_{LV}} \ln \left(\frac{h_m}{\delta l} \right). \quad (6.14)$$

Based on Eq. (6.13), we conduct parameter studies to examine the flow velocity $U_{\alpha s}$ at the boundary between LAL and bulk α phase. This velocity is influenced by the contact line radius r_c of phase α (droplet), droplet viscosity η , and capillary number Ca . The following parameters were applied: The apparent contact angle for the droplet phase α is set to $\theta_{app} = \pi/3$. The droplet viscosity $\eta = 10$ and the substrate velocity $U_0 = 1$ correspond to the capillary number $Ca = 0.1$. In figure 11(I), an increase in r_c means more frictional area. Consequently, the flow velocity $U_{\alpha s}$ rapidly converges to the no-slip condition, where $U_{\alpha s} = U_0$. Next, in figure 11(II), with the droplet size fixed at $r_c = 100$, we varied the droplet viscosity η from 1000 to 1. This highlights the interplay between droplet viscosity and droplet-solid friction. For an extremely viscous droplet at $\eta = 1000$, the high droplet-solid friction propels the droplet to move together with the substrate. However, this motion is simultaneously counteracted by droplet viscosity, which resists relative motion among the molecules of phase α . As a result, the slip behavior in LAL is highly dependent on both the droplet viscosity and droplet-solid interactions, such as bonding energy. In case study (III), we fix $\eta = 10$ and change the

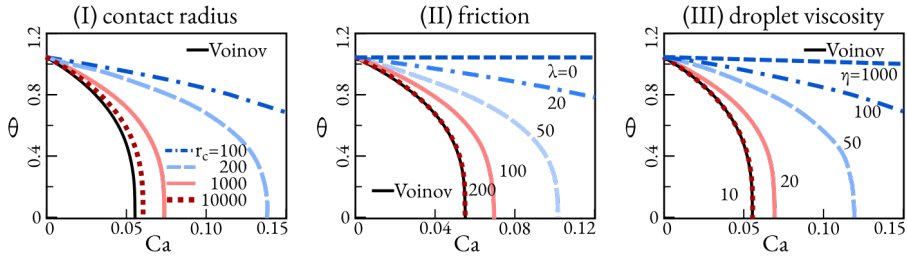


Figure 12: Contact angle θ deviates from the apparent contact angle $\theta_{\text{app}} = \pi/3$ at different capillary number Ca influenced by (I) droplet contact radius r_c ; (II) friction coefficient λ ; (III) droplet viscosity η . The black solid line denotes the Voinov relation Eq. (6.12).

capillary number Ca which is defined as

$$Ca = \frac{\eta U_0}{-\sigma_{LV}(\cos \theta - \cos \theta_{\text{app}})}.$$

Hence, the sign of Ca distinguishes two different scenarios: When $Ca > 0$, the thermodynamic force opposes the contact line movement relative to the substrate, leading to $\theta > \theta_{\text{app}}$ which corresponds to droplet advancing. When $Ca < 0$, the thermodynamic force facilitates the contact line motion along with the substrate, resulting in $\theta < \theta_{\text{app}}$ which occurs during droplet receding. However, these effects become significant only when friction is weak. As illustrated in figure 11(III), when the friction coefficient is sufficiently large ($\lambda > 100$), the flow velocity U_1 is primarily governed by friction. In such cases, surface tension has a negligible influence on the flow field near the triple junction, with friction emerging as the dominant factor controlling the local fluid dynamics.

By analyzing the flow velocity while considering both slip and friction in LAL, we examine the variation of the dynamic contact angle θ as a function of the capillary number Ca . As demonstrated in figure 12, noticeable deviations from the standard Cox-Voinov theory Eq. (6.12) (solid black lines) are observed. In figure 12(I), as the droplet contact radius r_c increases, the droplet-solid friction area expands. Only for significantly huge friction area, the Cox-Voinov tendency is recovered. Similarly, in figure 12(II), where the droplet-solid friction coefficient λ is varied, Cox-Voinov relation exhibits a positive correlation with λ . Notably, in the absence of friction at $\lambda = 0$, the contact angle remains constant and is entirely unaffected by the substrate. These results indicate that the no-slip boundary condition, as assumed in Cox-Voinov theory, is not an intrinsic property of the system but is fundamentally linked to friction. Friction plays a crucial role in transferring momentum from substrate molecules to the droplet molecules through intermolecular forces, thereby inducing internal fluid motion within the droplet. This flow field generates viscous stress, modifies the curvature of the droplet-air interface, and ultimately leads to deviations from Young's law.

While friction acts as the primary driver of momentum transfer, viscous stress counteracts the internal flow of the droplet. In figure 12(III), we set $r_c = 100$, $\lambda = 20$ and vary the droplet viscosity η . Standard Cox-Voinov theory primarily considers the viscous effects in the bulk droplet region; however, we emphasize that viscosity within LAL is also critical, as it governs kinetic energy dissipation through fluid molecular interactions. For highly viscous droplets, friction alone cannot overcome the viscous stress in LAL, leading to rapid energy dissipation that prevents effective momentum transfer to the bulk droplet. Conversely, for less viscous droplets, where friction becomes more dominant, the Cox-Voinov behavior is recovered, suggesting an effective equivalence to the no-slip boundary condition. Thus, slip behavior is not an absolute property but rather a consequence of the interplay between the

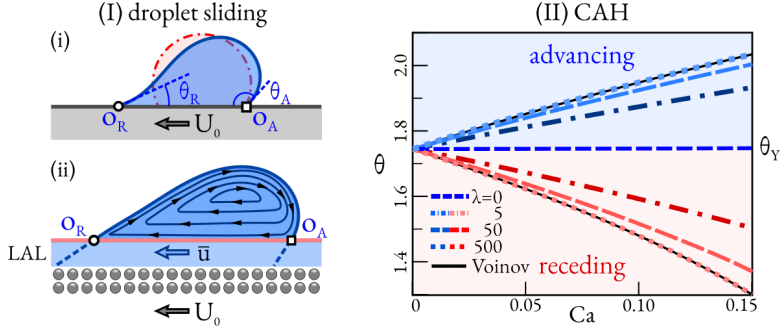


Figure 13: Contact angle hysteresis as droplet slides: (I)(i) macroscopic: the left-moving solid substrate (U_0) deforms the droplet (blue), leading to the advancing/receding contact angles θ_A/θ_R deviating from Young's angle $\theta_Y = 5\pi/9$, (ii) microscopic: illustration of the droplet internal flow field induced by sliding; (II) CAH with increase in the capillary number Ca at droplet viscosity $\eta = 100$, compared with Voinov theory (black solid lines). No CAH is observed for zero friction coefficient λ .

friction at droplet-solid and the viscous effect of droplet molecules. For instance, a highly viscous droplet does not necessarily exhibit the no-slip condition; its interaction with the substrate also plays a determining role.

6.4. Droplet sliding with friction force

We now examine how friction forces affect droplet sliding. As illustrated in figure 13(I)(i), when the substrate moves leftward, the receding contact angle θ_R forms at the left triple junction O_R , and the advancing contact angle θ_A appears at the right triple junction O_A , both deviate from the equilibrium Young's angle θ_Y .

For small capillary number Ca , we adopt the stagnation assumption for the triple junctions, following the study of Qian *et al.* (2006). That is, although the triple junctions remain stationary, an internal flow field develops inside the droplet, as depicted in figure 13(I)(ii). According to Voinov's theory, this internal flow induces viscous stresses that must be balanced by surface tension, leading to contact angle hysteresis. However, in previous models, the velocity at the droplet-substrate interface is assumed to be equal to the substrate velocity U_0 , corresponding to the no-slip boundary condition. In this work, we challenge this assumption by arguing that the fluid flow at the droplet-substrate interface follows a more complex evolution, governed by the interplay of friction, viscous stresses, and surface tension. We investigate how this balance influences droplet motion and how deviations from the no-slip condition impact the overall wetting dynamics.

By setting the droplet viscosity to $\eta = 100$, the standard Voinov theory Eq. (6.12) captures the CAH with increasing capillary number Ca , which is depicted by the solid black lines in figure 13(II). However, when incorporating droplet-solid friction in the LAL, we find that the friction parameter λ significantly influence CAH. Notably, the dynamic contact angle converges to Voinov's theoretical prediction only under strong droplet-solid friction. This suggests that friction plays a crucial role in transferring momentum from the moving substrate to the droplet, which drives the internal fluid motion. At $\lambda = 0$ (i.e., in the absence of friction), the momentum transfer is negligible, resulting in an extremely weak internal flow. Consequently, the viscous stress becomes minimal, preventing significant curvature variation at the contact line. As a result, CAH vanishes entirely.

With our theory, we write the force balance for the whole sliding droplet with the mass m^*

by considering the friction force at the droplet-solid interface,

$$\mathbf{F}_{\text{crit}} = m^* \frac{d\mathbf{U}}{dt} = 2 \int_0^\pi \int_0^{r_c \cos \xi} [\lambda(\mathbf{u} - \mathbf{U}_0) - \eta \partial_n \mathbf{u} - \eta \partial_{xx} \mathbf{u} - \bar{c} \partial_x \bar{\mu}] dx d\xi.$$

Letting $d\mathbf{U}/dt = 0$, the critical friction force \mathbf{F}_{crit} is composed of three parts. The first contributor is the kinetics induced friction \mathbf{F}_{kin} ,

$$\mathbf{F}_{\text{kin}} = 2 \int_0^\pi \int_0^{r_c \cos \xi} \lambda(\mathbf{u} - \mathbf{U}_0) dx d\xi = -2\pi r_c \lambda \mathbf{U}_0 / \beta,$$

where the solid-fluid friction is scaled by the contact line length $2\pi r_c$ and propels the droplet motion with the substrate. The second contributor is the viscous drag force from the bulk fluid above \mathbf{F}_{drag} ,

$$\mathbf{F}_{\text{drag}} = 2 \int_0^\pi \int_0^{r_c \cos \xi} (-\eta \partial_n \mathbf{u} - \eta \partial_{xx} \mathbf{u}) dx d\xi = 2\pi r_c \eta \beta \mathbf{U}_0,$$

where the solid-fluid friction is scaled by the contact line length $2\pi r_c$ and propels the droplet motion with the substrate. The last contributor is the capillary induced friction \mathbf{F}_{cap} ,

$$\mathbf{F}_{\text{cap}} = 2 \int_0^\pi \int_0^{r_c \cos \xi} -\bar{c} \partial_x \bar{\mu} dx d\xi = 2 r_c \sigma_{\text{LV}} (\cos \theta_R - \cos \theta_A),$$

which is consistent with the Kawasaki-Furmidge equation (Kawasaki 1960; Furmidge 1962; Li *et al.* 2023) and resists the droplet slide.

7. Conclusion

In this work, we investigate the fundamental physical mechanisms underlying no-slip, as well as partial-slip boundary conditions by examining the interplay between hydrodynamics and thermodynamics in multi-component fluids in contact with solid substrates. We introduce the Langmuir adsorption layer (LAL) as a crucial interfacial region where solid-fluid intermolecular interactions not only drive depletion/adsorption phenomena, reducing chemical free energy, but also induce fluid motion to minimize kinetic energy.

Using energy minimization principles, we derive the force balance framework in LAL, revealing the critical role of solid-fluid friction in governing slip behavior. From a molecular perspective, we propose that friction originates from the elongation, shortening, and rotation of solid-fluid bonds, which resist molecular slip. Consequently, the magnitude of the friction force \mathbf{F} is intrinsically linked to the solid-fluid bonding energy, rather than the flow geometry. LAL thus serves as a crucial transition zone between the solid substrate and bulk fluid, where energy dissipation occurs through both hydrodynamic and thermodynamic processes.

Extending our framework to classical fluid flow problems, including single-phase flow and Huh & Scriven wedge flow, we demonstrate that solid-fluid friction in LAL acts as a key mechanism for momentum transfer which modifies bulk fluid flow, making slip behavior an emergent property governed by the interplay of interfacial tension, solid-fluid friction, and bulk viscosity. These findings challenge classical mathematical no-slip condition where steady-state velocity profile is typically predefined but may not always be physically justified.

Furthermore, by incorporating the Cox-Voinov theory with slip for droplet sliding, we reveal that solid-fluid friction strongly influences droplet internal flow near the triple junction and directly contributes to contact angle hysteresis (CAH) derivation from the standard Cox-

Voinov theory:

$$\theta^3 = \theta_{\text{app}}^3 + \frac{-2\sigma_{\text{LV}}(\cos \theta - \cos \theta_{\text{app}}) + (\lambda/\beta + \eta\beta)U_0 + \lambda U_0 r_c}{4\eta/(\lambda\beta) - \lambda/\beta - \eta\beta + \lambda r_c} \frac{9\eta}{\sigma_{\text{LV}}} \ln \left(\frac{h_m}{\delta l} \right),$$

where the friction significantly impacts the internal droplet flow, modifies the viscous stress across the droplet surface, and deforms the droplet dynamic contact angle θ deviating from the apparent Young's angle θ_{app} .

Starting from the force balance equation in the adsorption layer, the critical friction force for the droplet slide is deduced as a combination of:

- Capillary induced friction $\mathbf{F}_{\text{cap}} = 2 r_c \sigma_{\text{LV}} (\cos \theta_{\text{R}} - \cos \theta_{\text{A}})$ related with surface tension σ_{LV} ;
- fluid viscous drag force $\mathbf{F}_{\text{drag}} = 2\pi r_c \eta \beta \mathbf{U}_0$ depending on the fluid viscosity η ;
- Kinetics induced friction $\mathbf{F}_{\text{kin}} = -2\pi r_c \lambda \mathbf{U}_0 / \beta$ scaled by the contact line length $2\pi r_c$.

Future research could further expand our model by incorporating: temperature gradients (Marangoni effects) to explore thermally induced slip, electric fields (electrowetting) to study charge-driven wetting behavior, and more complex multi-scale interactions across solid, liquid, and gas phases. Additionally, validations via experiments and molecular dynamics simulations and advanced imaging techniques would provide deeper insights into the microscopic origins of slip, friction, and energy dissipation at fluid-solid interfaces. By refining our understanding of wetting and interfacial slip, this work lays the foundation for advancements in microfluidics, coatings, and droplet-based technologies.

Fundings

This work was supported by the Gottfried-Wilhelm Leibniz prize NE 822/31-1 of the German research foundation (DFG), VirtMat project P09 “Wetting Phenomena” of the Helmholtz Association (MSE-programme No. 43.31.01).

Declaration of interests

The authors report no conflict of interest.

REFERENCES

- ALIPOUR, PEDRAM, TOGHRAIE, DAVOOD, KARIMPOUR, ARASH & HAJIAN, MEHDI 2019 Molecular dynamics simulation of fluid flow passing through a nanochannel: effects of geometric shape of roughnesses. *Journal of Molecular Liquids* **275**, 192–203.
- AMIRFAZLI, A & NEUMANN, AW 2004 Status of the three-phase line tension: a review. *Advances in colloid and interface science* **110** (3), 121–141.
- BAE, HYUNJI JANE, LOZANO-DURÁN, ADRIÁN, BOSE, SANJEEB T & MOIN, PARVIZ 2019 Dynamic slip wall model for large-eddy simulation. *Journal of fluid mechanics* **859**, 400–432.
- BOCQUET, LYDÉRIC & BARRAT, JEAN-LOUIS 1994 Hydrodynamic boundary conditions, correlation functions, and kubo relations for confined fluids. *Physical review E* **49** (4), 3079.
- BUI, ANNA T & COX, STEPHEN J 2024 Revisiting the green–kubo relation for friction in nanofluidics. *The Journal of Chemical Physics* **161** (20).
- BUTT, HANS-JÜRGEN, BERGER, RÜDIGER, STEFFEN, WERNER, VOLLMER, DORIS & WEBER, STEFAN AL 2018 Adaptive wetting—adaptation in wetting. *Langmuir* **34** (38), 11292–11304.
- CAHN, JOHN W & HILLIARD, JOHN E 1958 Free energy of a nonuniform system. i. interfacial free energy. *The Journal of chemical physics* **28** (2), 258–267.
- CAI, YUHAN, WANG, FEI, ZHANG, HAODONG & NESTLER, BRITTA 2024 Chemo-elasto-electro free energy of non-uniform system in the diffuse interface context. *Journal of Physics: Condensed Matter* **36** (49), 495702.

- CHRISTIANO, RAYMOND, RAHMAWAN, YUDI, SEMPREBON, CIRO & KUSUMAATMAJA, HALIM 2022 Modeling the dynamics of partially wetting droplets on fibers. *Physical Review Fluids* **7** (10), 103606.
- CORON, JEAN-MICHEL 1996 On the controllability of the 2-d incompressible navier-stokes equations with the navier slip boundary conditions. *ESAIM: Control, Optimisation and Calculus of Variations* **1**, 35–75.
- COX, RG 1986 The dynamics of the spreading of liquids on a solid surface. part 1. viscous flow. *Journal of fluid mechanics* **168**, 169–194.
- CROSS, BENJAMIN, BARRAUD, CHLOÉ, PICARD, CYRIL, LÉGER, LILIANE, RESTAGNO, FRÉDÉRIC & CHARLAIX, ÉLISABETH 2018 Wall slip of complex fluids: Interfacial friction versus slip length. *Physical Review Fluids* **3** (6), 062001.
- DE GENNES, PIERRE GILLES 1981 Polymer solutions near an interface. adsorption and depletion layers. *Macromolecules* **14** (6), 1637–1644.
- DE GENNES, PIERRE-GILLES 1985 Wetting: statics and dynamics. *Reviews of modern physics* **57** (3), 827.
- DING, GUANG-YU & XIA, KE-QING 2023 Heat transport and flow morphology of geostrophic rotating rayleigh–bénard convection in the presence of boundary flow. *Journal of Fluid Mechanics* **975**, A46.
- FURMIDGE, CGL 1962 Studies at phase interfaces. i. the sliding of liquid drops on solid surfaces and a theory for spray retention. *Journal of colloid science* **17** (4), 309–324.
- GIBBS, JOSIAH WILLARD 1928 *The Collected Works of J. Willard Gibbs...: Thermodynamics*, , vol. 1. Longmans, Green and Company.
- HADJICONSTANTINO, NG 2021 An atomistic model for the navier slip condition. *Journal of Fluid Mechanics* **912**, A26.
- HADJICONSTANTINO, NICOLAS G 2024 Molecular mechanics of liquid and gas slip flow. *Annual Review of Fluid Mechanics* **56** (1), 435–461.
- JACQMIN, DAVID 2000 Contact-line dynamics of a diffuse fluid interface. *Journal of fluid mechanics* **402**, 57–88.
- JOSEPH, PIERRE & TABELING, PATRICK 2005 Direct measurement of the apparent slip length. *Physical Review E—Statistical, Nonlinear, and Soft Matter Physics* **71** (3), 035303.
- JUNG, TAEYONG, CHOI, HAECHEON & KIM, JOHN 2016 Effects of the air layer of an idealized superhydrophobic surface on the slip length and skin-friction drag. *Journal of Fluid Mechanics* **790**, R1.
- KAWASAKI, KOJI 1960 Study of wettability of polymers by sliding of water drop. *Journal of Colloid Science* **15** (5), 402–407.
- KRÜGER, TIMM, KUSUMAATMAJA, HALIM, KUZMIN, ALEXANDR, SHARDT, OREST, SILVA, GONCALO & VIGGEN, ERLEND MAGNUS 2017 The lattice boltzmann method. *Springer International Publishing* **10** (978-3), 4–15.
- KUMAR KANNAM, SRIDHAR, TODD, BD, HANSEN, JESPER SCHMIDT & DAIVIS, PETER J 2012 Slip length of water on graphene: Limitations of non-equilibrium molecular dynamics simulations. *The Journal of chemical physics* **136** (2).
- KUSUMAATMAJA, HALIM, HEMINGWAY, EWAN J & FIELDING, SUZANNE M 2016 Moving contact line dynamics: from diffuse to sharp interfaces. *Journal of Fluid Mechanics* **788**, 209–227.
- LAUGA, ERIC, BRENNER, MICHAEL P & STONE, HOWARD A 2005 Microfluidics: the no-slip boundary condition. *arXiv preprint cond-mat/0501557* .
- LAUGA, ERIC & STONE, HOWARD A 2003 Effective slip in pressure-driven stokes flow. *Journal of Fluid Mechanics* **489**, 55–77.
- LAW, BRUCE M, MCBRIDE, SEAN P, WANG, JIANG YONG, WI, HAENG SUB, PANERU, GOVIND, BETELU, SANTIGO, USHIJIMA, BAKU, TAKATA, YOUICHI, FLANDERS, BRET, BRESME, FERNANDO & OTHERS 2017 Line tension and its influence on droplets and particles at surfaces. *Progress in surface science* **92** (1), 1–39.
- LI, XIAOMEI, BODZIONY, FRANCISCO, YIN, MARIANA, MARSCHALL, HOLGER, BERGER, RÜDIGER & BUTT, HANS-JÜRGEN 2023 Kinetic drop friction. *Nature Communications* **14** (1), 4571.
- LIM, ZI LI, CHONG, KAI LEONG, DING, GUANG-YU & XIA, KE-QING 2019 Quasistatic magnetoconvection: heat transport enhancement and boundary layer crossing. *Journal of Fluid Mechanics* **870**, 519–542.
- LIU, XINYU, SHEN, JIE & ZHENG, NAN 2024 Efficient energy stable numerical schemes for cahn–hilliard equations with dynamical boundary conditions. *Journal of Computational Physics* **509**, 113037.
- LUCHINI, PAOLO 2013 Linearized no-slip boundary conditions at a rough surface. *Journal of fluid mechanics* **737**, 349–367.
- MAALI, ABDELHAMID & BHUSHAN, BHARAT 2012 Measurement of slip length on superhydrophobic surfaces.

- Philosophical Transactions of the Royal Society A: Mathematical, Physical and Engineering Sciences* **370** (1967), 2304–2320.
- MAXWELL, JAMES CLERK 1879 Vii. on stresses in rarified gases arising from inequalities of temperature. *Philosophical Transactions of the royal society of London* (170), 231–256.
- MOFFATT, H KEITH 1964 Viscous and resistive eddies near a sharp corner. *Journal of Fluid Mechanics* **18** (1), 1–18.
- MORI, HAZIME 1965 Transport, collective motion, and brownian motion. *Progress of theoretical physics* **33** (3), 423–455.
- MURALIDHAR, PRANESH, FERRER, NANGELIE, DANIELLO, ROBERT & ROTHSTEIN, JONATHAN P 2011 Influence of slip on the flow past superhydrophobic circular cylinders. *Journal of Fluid Mechanics* **680**, 459–476.
- MYERS, TIM G 2011 Why are slip lengths so large in carbon nanotubes? *Microfluidics and nanofluidics* **10**, 1141–1145.
- NAVIER, CLAUDE 1822 *Mémoire sur les lois du mouvement des fluides*. éditeur inconnu.
- NETO, CHIARA, EVANS, DREW R, BONACCURSO, ELMAR, BUTT, HANS-JÜRGEN & CRAIG, VINCENT SJ 2005 Boundary slip in newtonian liquids: a review of experimental studies. *Reports on progress in physics* **68** (12), 2859.
- PETRAVIC, JANKA & HARROWELL, PETER 2007 On the equilibrium calculation of the friction coefficient for liquid slip against a wall. *The Journal of chemical physics* **127** (17).
- QIAN, TIEZHENG, QIU, CHUNYIN & SHENG, PING 2008 A scaling approach to the derivation of hydrodynamic boundary conditions. *Journal of Fluid Mechanics* **611**, 333–364.
- QIAN, TIEZHENG, WANG, XIAO-PING & SHENG, PING 2003 Molecular scale contact line hydrodynamics of immiscible flows. *Physical Review E* **68** (1), 016306.
- QIAN, TIEZHENG, WANG, XIAO-PING & SHENG, PING 2004 Power-law slip profile of the moving contact line in two-phase immiscible flows. *Physical review letters* **93** (9), 094501.
- QIAN, TIEZHENG, WANG, XIAO-PING & SHENG, PING 2006 A variational approach to moving contact line hydrodynamics. *Journal of Fluid Mechanics* **564**, 333–360.
- RAMOS-ALVARADO, BLADIMIR, KUMAR, SATISH & PETERSON, GP 2016 Hydrodynamic slip length as a surface property. *Physical Review E* **93** (2), 023101.
- REN, WEIQING, TRINH, PHILIPPE H & WEINAN, E 2015 On the distinguished limits of the navier slip model of the moving contact line problem. *Journal of Fluid Mechanics* **772**, 107–126.
- SCHIMMELE, L, NAPIÓRKOWSKI, M & DIETRICH, S 2007 Conceptual aspects of line tensions. *The Journal of chemical physics* **127** (16).
- SECCHI, ELEONORA, MARBACH, SOPHIE, NIGUÈS, ANTOINE, STEIN, DEREK, SIRIA, ALESSANDRO & BOCQUET, LYDÉRIC 2016 Massive radius-dependent flow slippage in carbon nanotubes. *Nature* **537** (7619), 210–213.
- SHIMIZU, JUN, EDA, HIROSHI, YORITSUNE, MASASHI & OHMURA, ETSUJI 1998 Molecular dynamics simulation of friction on the atomic scale. *Nanotechnology* **9** (2), 118.
- VOINOV, OLEG V 1976 Hydrodynamics of wetting. *Fluid dynamics* **11** (5), 714–721.
- VORONOV, ROMAN S, PAPAVALSILIOU, DIMITRIOS V & LEE, LLOYD L 2006 Boundary slip and wetting properties of interfaces: Correlation of the contact angle with the slip length. *The Journal of chemical physics* **124** (20).
- WANG, FEI & NESTLER, BRITTA 2024a Compressible and immiscible fluids with arbitrary density ratio. *arXiv preprint arXiv:2406.19786* .
- WANG, FEI & NESTLER, BRITTA 2024b Wetting and contact-angle hysteresis: Density asymmetry and van der waals force. *Physical Review Letters* **132** (12), 126202.
- WANG, FEI, ZHANG, HAODONG & NESTLER, BRITTA 2024 Wetting phenomena: Line tension and gravitational effect. *Physical Review Letters* **133** (24), 246201.
- WANG, FEI, ZHANG, HAODONG, WU, YANCHEN & NESTLER, BRITTA 2023 A thermodynamically consistent diffuse interface model for the wetting phenomenon of miscible and immiscible ternary fluids. *Journal of Fluid Mechanics* **970**, A17.
- WEN, BAOLE, GOLUSKIN, DAVID & DOERING, CHARLES R 2022 Steady rayleigh–bénard convection between no-slip boundaries. *Journal of Fluid Mechanics* **933**, R4.
- XIA, KE-QING 2024 Unveiling the mystery of effective slip. *Journal of Fluid Mechanics* **1000**, F5.
- XIE, QUAN, ALIBAKHSI, MOHAMMAD AMIN, JIAO, SHUPING, XU, ZHIPING, HEMPEL, MAREK, KONG, JING, PARK, HYUNG GYU & DUAN, CHUANHUA 2018 Fast water transport in graphene nanofluidic channels. *Nature nanotechnology* **13** (3), 238–245.

- XU, XIANMIN, DI, YANA & YU, HAIJUN 2018 Sharp-interface limits of a phase-field model with a generalized navier slip boundary condition for moving contact lines. *Journal of Fluid Mechanics* **849**, 805–833.
- YARIV, E 2023 Effective slip length for transverse shear flow over partially invaded grooves. *Journal of Fluid Mechanics* **957**, R1.
- YUE, PENGTAO 2020 Thermodynamically consistent phase-field modelling of contact angle hysteresis. *Journal of Fluid Mechanics* **899**, A15.
- YUE, PENGTAO & FENG, JAMES J 2012 Phase-field simulations of dynamic wetting of viscoelastic fluids. *Journal of Non-Newtonian Fluid Mechanics* **189**, 8–13.
- YUE, PENGTAO, FENG, JAMES J, LIU, CHUN & SHEN, JIE 2004 A diffuse-interface method for simulating two-phase flows of complex fluids. *Journal of Fluid Mechanics* **515**, 293–317.
- YUE, PENGTAO, ZHOU, CHUNFENG & FENG, JAMES J 2010 Sharp-interface limit of the cahn–hilliard model for moving contact lines. *Journal of Fluid Mechanics* **645**, 279–294.
- ZHANG, HAODONG, WANG, FEI & NESTLER, BRITTA 2022 Janus droplet formation via thermally induced phase separation: a numerical model with diffusion and convection. *Langmuir* **38** (22), 6882–6895.
- ZHANG, HAODONG, WANG, FEI & NESTLER, BRITTA 2023 Line tension of sessile droplets: Thermodynamic considerations. *Physical Review E* **108** (5), 054121.
- ZHANG, HAODONG, WANG, FEI & NESTLER, BRITTA 2024a Multi-component electro-hydro-thermodynamic model with phase-field method. i. dielectric. *Journal of Computational Physics* p. 112907.
- ZHANG, HAODONG, WANG, FEI, RATKE, LORENZ & NESTLER, BRITTA 2024b Brownian motion of droplets induced by thermal noise. *Physical Review E* **109** (2), 024208.
- ZHANG, HAODONG, WU, YANCHEN, WANG, FEI, GUO, FUHAO & NESTLER, BRITTA 2021 Phase-field modeling of multiple emulsions via spinodal decomposition. *Langmuir* **37** (17), 5275–5281.
- ZHANG, HAODONG, ZHANG, HONGMIN, WANG, FEI & NESTLER, BRITTA 2024c Wetting effect induced depletion and adsorption layers: Diffuse interface perspective. *ChemPhysChem* p. e202400086.
- ZWANZIG, ROBERT 1961 Memory effects in irreversible thermodynamics. *Physical Review* **124** (4), 983.